Aerospace Science and Technology 146 (2024) 108929

Contents lists available at ScienceDirect

Aerospace Science and Technology

journal homepage: www.elsevier.com/locate/aescte

Evaluation of dynamic loads and performance indexes in tiltrotors using a mid-fidelity aeroservoelastic tool

Alberto Savino [a,*], Alessandro Cocco [b], Vincenzo Muscarello [c]

[a] Dipartimento di Scienze e Tecnologie Aerospaziali, Politecnico di Milano, via La Masa 34, Milan, 20156, Italy
[b] Department of Aerospace Engineering, University of Maryland, 3182 Glenn L. Martin Hall, College Park, 20740, MD, United States
[c] Aerospace Engineering and Aviation, Royal Melbourne Institute of Technology, 264 Plenty Road, Melbourne, 3082, VIC, Australia

ARTICLE INFO

Communicated by George Barakos

Keywords:
Aeroelasticity
Fluid-structure interaction
Tiltrotor
VTOL
Mid-fidelity aerodynamics
Multibody dynamics

ABSTRACT

This work presents a comprehensive numerical environment, obtained by the coupling of a mid-fidelity aerodynamic solver based on a vortex particle method with a multibody dynamics tool, for aeroelastic simulations suitable for the analysis and design of next-generation rotary-wing aircraft. Indeed, the presence of multiple propellers and rotors, together with interactional aerodynamics, have a strong impact on dynamic loads and performance indexes on rotorcraft. A mid-fidelity approach provides an ideal trade-off between the accuracy of the solution and the speed of execution required in the preliminary design phases of these vehicles.
A tiltrotor model representative of the Bell XV-15 with different levels of complexity is proposed as a test benchmark, whose characteristics can be similar to an eVTOL. The coupled solver shows the capability to determine the trim conditions in airplane mode and predicts steady and periodic trim loads. Transient analyses are presented as well, considering a roll maneuver and highlighting the importance of the accurate representation of rotary wing aerodynamics provided by the vortex particle method for load evaluation and vibrational assessment.

1. Introduction

In the ever-evolving world of aeronautics, researchers and engineers constantly strive to develop reliable numerical methods with multiple levels of sophistication, while maintaining an appropriate balance between accuracy and computational efficiency. The development of next-generation vehicles, including tiltrotors and electric Vertical Take-Off and Landing (eVTOL) vehicles [1], poses a challenge for engineers due to the increasing demands of mission objectives and safety regulations.

The design of rotary-wing aircraft requires to identify the critical aspects that this type of configuration presents. Indeed, these vehicles have shown great promise, but they are not without their obstacles. One of the most significant hurdles these configurations encounter is the issue of costs. Rotorcraft are complex vehicles, comprising numerous moving parts. As a result, their operation and maintenance costs can be prohibitively high. This poses a considerable barrier, particularly for commercial applications, where cost-effectiveness plays a pivotal role in decision-making. Another area of concern is due to the noise generated by rotating components. For example, when tiltrotor aircraft transition into helicopter mode during takeoff and landing, they rely on dual rotors, which inherently generate more noise compared to traditional helicopters. Moreover, general VTOL configurations with multiple rotors create a considerable amount of noise due to their high rotational speed. Noise can be a significant problem, especially in the urban environment, where acoustic pollution can have adverse effects on communities [2,3]. Furthermore, we must not overlook the regulatory challenges tiltrotors and newer VTOL aircraft face. Although the concept of tiltrotors is not entirely new, establishing comprehensive guidelines from a regulatory standpoint remains a complex task. The situation becomes even more critical for the emerging eVTOL aircraft designs. Governments and aviation authorities must work together to define safety standards, certification processes, and air traffic control systems that ensure the safe integration of these aircraft into our

* Corresponding author.
E-mail address: alberto.savino@polimi.it (A. Savino).

https://doi.org/10.1016/j.ast.2024.108929
Received 3 November 2023; Received in revised form 22 December 2023; Accepted 24 January 2024

Nomenclature

$\boldsymbol{x}$	kinematics unknowns	δ_a	flaperon deflection
$\boldsymbol{p}$	momentum unknowns	T_z	vertical reaction force
λ	Lagrangian multipliers	M_y	pitching moment
$\boldsymbol{M}$	inertia matrix	ϕ	bank angle
$\boldsymbol{f}_i$	internal forces	$\dot{\phi}$	roll rate
$\boldsymbol{f}_e$	external forces	ψ	blade azimuth angle
$\boldsymbol{\phi}(\boldsymbol{x})$	kinematics holonomic constraints	θ_{75}	blade pitch angle at 75% of rotor radius
$\boldsymbol{\phi}_{/x}$	Jacobian matrix with respect to kinematics unknowns	b	wing span
$\boldsymbol{F}_{\text{act}}$	actuation force	b_t	horizontal tailplane span
K_a	actuator stiffness	U_∞	free-stream velocity
C_a	actuator damping	R_{75}	75% of rotor radius
ΔL	actuator length	ω	rotor angular velocity
θ	aircraft pitch angle	α^r_{R75}	blade angle of attack at 75% of rotor radius, right rotor
δ	elevator deflection	α^l_{R75}	blade angle of attack at 75% of rotor radius, left rotor

airspace. Last but not least, is the safety factor. Tiltrotors are relatively new compared to conventional helicopters, and their safety record is being scrutinized. In recent years, there have been accidents involving tiltrotors, such as the unfortunate V-22 crash in June 2022 and the incident involving the AW609 [4]. In general, new-generation rotorcraft can transform aviation in multiple ways. However, before they can be extensively utilized for commercial and military purposes, several obstacles and constraints need to be resolved. With additional research and development, it is probable that these difficulties will be tackled, ultimately paving the path for the broader utilization of this potential technology.

One of the major challenges from a preliminary-intermediate design perspective is the ability to conduct comprehensive aeroelastic simulations that consider the interplay between the aerodynamics and the structural dynamics of the vehicle. This capability is vital for the advancement of new aircraft designs [5].

Advanced numerical techniques have been developed to aid in the examination of various flight conditions commonly encountered by rotorcraft. These tools provide a higher level of accuracy and precision as the level of detail increases. Indeed, a substantial effort was spent in the past years to develop computational structural dynamics (CSD) tools that were effectively used for rotorcraft applications (e.g. [6–8]). Structural dynamics of rotary-wing vehicles were typically investigated using the multibody approach [9,10], which takes into account the nonlinear dynamics of the interconnected rigid and flexible bodies representing the aircraft components. The multibody approach is commonly used to study aeroelastic phenomena, particularly for whirl-flutter instabilities that may arise in tiltrotors in high-speed airplane mode flight [11,12]. A significant effort in this research field was spent at Politecnico di Milano, where starting in the 1990s a free general-purpose multibody software called MBDyn[1] was developed [13]. However, most multibody solvers, like MBDyn, use simplified aerodynamic models based on Blade Element Momentum Theory (BEMT). These models do not account for the aerodynamic interactions between rotors and the actual geometry of lifting surfaces, resulting in an inaccurate representation of the aerodynamic loads and a loss of information related to periodic actions. To overcome this limitation, a more accurate and detailed aerodynamic model should be used.

The coupling of CSD tools with high-fidelity computational fluid dynamics (CFD) solvers was successfully investigated and implemented in the last two decades for rotorcraft aeroelastic simulations [14–19] including, for example, the flutter calculations of a vertical tail model [20] and for the analysis of rotor blade structural loads of a complete helicopter model tested in a transonic wind tunnel [21]. Nevertheless, despite continuous advances in the field of high-performance computing, the coupled CSD/CFD simulations still require a significant computational effort, not suitable for the preliminary design stage of novel VTOL configurations, which requires a great number of simulations to reproduce the different flight conditions that characterize their mission.

To address this challenge, mid-fidelity tools are emerging as an optimal trade-off between computational cost and desired accuracy, particularly in the early design stages. While computational fluid dynamics methods can analyze the unsteady interactions, the resolution of wake dynamics in conventional CFD tools requires high-order numerical schemes and mesh resolutions that are computationally expensive, making them unsuitable for design space exploration. To cite a few examples, Lu et al. [22] developed an optimization methodology for a helicopter design based on a viscous Vortex Particle Method (VPM) model combined with an unsteady panel hybrid method. Alvarez and Ning developed a VPM-based code [23] for the investigation of multirotor configurations. Tan et al. [24] used a vortex-based approach coupled with a viscous boundary model to study rotor-to-rotor interactional problems occurring during shipboard operations.

Recently, Politecnico di Milano developed a mid-fidelity computational tool, called DUST[2] aimed at representing a fast and reliable asset for the simulation of the aerodynamics of complex rotorcraft configurations [25].

The present work proposes the combination of the multibody solver MBDyn with the mid-fidelity aerodynamic tool DUST, aiming at representing an ideal trade-off between speed of execution and accuracy of the solution, devoted to the analysis and the preliminary design phase of novel rotary-wing aircraft configurations. The coupling of the two codes relies on the partitioned multi-physics coupling library preCICE [26]. An interesting novelty proposed by this tool is the capability of modeling the control surfaces, representing an essential aspect for the simulation of aircraft maneuvers. The coupled code has been presented and validated in Ref. [27]. The proposed approach allows us to: 1) develop numerical models with several levels of complexity to highlight the impact of the different components on performance, stability, and loads; 2) perform comprehensive analyses in the same environment including trim, maneuver, and flutter/whirl-flutter; 3) determine steady and periodic loads, useful for vibratory assessment and fatigue life analysis; 4) evaluate the impact of the elastic components on system dynamics.

Thanks to a large amount of public data, the XV-15 tiltrotor equipped with Advanced Technology Blade (ATB) is chosen as the benchmark model [28–31]. A vehicle like a tiltrotor allows us to show-

[1] https://public.gitlab.polimi.it/DAER/mbdyn, visited on August 2023.

[2] https://public.gitlab.polimi.it/DAER/dust, visited on August 2023.

case the capabilities of the methodology as the aircraft combines the typical challenges of both fixed-wing and rotary-wing at the same time.

The paper proceeds as follows: section 2 briefly presents the multibody and the mid-fidelity aerodynamic tools from a theoretical perspective. Section 3 describes the aeroservoelastic model of the XV-15, including validations with experimental data and high-fidelity CFD simulations. Section 4 describes the procedure to trim the aircraft in a steady-level flight as well as the roll maneuver. Section 5 summarizes the results obtained from the coupled simulations, highlighting the impact of mid-fidelity aerodynamics on the evaluation of dynamic loads and performance indexes of the aircraft. The last section brings the paper to closure by drawing conclusions about the work performed.

2. Numerical environment

2.1. Mid-fidelity aerodynamic solver: DUST

DUST is an open-source code, released under MIT license, that integrates different aerodynamic models for solid bodies, such as thick surface panels, thin vortex lattice elements, and lifting line elements. Moreover, a vortex particle method was implemented for wake modeling that provides a stable description of the free-vorticity flow field, which is suitable for numerical simulations of configurations characterized by strong aerodynamic interactions.

The mathematical formulation relies on a vorticity-velocity mixed aerodynamic problem, founded on the Helmholtz decomposition of the velocity field and a Lagrangian description of the vorticity field. The problem, based on the incompressible flow hypothesis, is formulated by using Helmholtz's decomposition of the velocity field that is given by the irrotational and solenoidal contributions of velocity.

A DUST model only requires surface meshes as the core of the mid-fidelity aerodynamic code is the vortex particle method (VPM) [32,33] implemented for the wake modeling that provides a stable Lagrangian description of the free-vorticity flow field. The Lagrangian grid-free approach does not require a volume mesh of the surrounding flow. The vortex particle method effectively captures the interaction of wakes produced by lifting surfaces and bodies, as is commonly seen in rotary-wing vehicle applications. To reduce computational costs associated with vortex particle interactions, a Cartesian Fast Multipole Method (FMM) [34,35] is employed.

The code computes aerodynamic loads using a different approach based on the type of element chosen to model the problem. For lifting line elements, the aerodynamic loads are determined from the tabulated sectional aerodynamic coefficients, which are used to calculate their intensity. For vortex lattice elements, the aerodynamic loads are computed using the unsteady version of the Kutta-Joukowsky theorem. For surface panel elements, the aerodynamic loads are determined through the unsteady formulation of Bernoulli's theorem, taking into account the vorticity of the flow.

2.2. Multibody solver: MBDyn

MBDyn is a free general-purpose multibody solver developed at Politecnico di Milano. The tool automatically writes and solves the equations of motion of a system of entities possessing degrees of freedom (nodes) connected through algebraic constraints and subjected to internal and external loads. Constraint equations are explicitly accounted for, following a redundant coordinate set approach. Thus, the resulting system of Differential-Algebraic Equations (DAE) takes the Hessenberg form:

$$\mathbf{M}(\mathbf{x},t)\dot{\mathbf{x}} = \mathbf{p} \tag{1a}$$

$$\dot{\mathbf{p}} = \boldsymbol{\phi}_{/\mathbf{x}}^{T}\lambda + \mathbf{f}_i(\dot{\mathbf{x}},\mathbf{x},t) + \mathbf{f}_e(\dot{\mathbf{x}},\mathbf{x},t) \tag{1b}$$

$$\mathbf{0} = \boldsymbol{\phi}(\mathbf{x}) \tag{1c}$$

Table 1
XV-15 general characteristics.

Characteristic	Symbol	XV-15 (ATBs)	Units
Gross takeoff weight	W_{TO}	13,000	lb
Maximum engine(s) power	P_{max}	2×1,550	hp
Maximum flight speed	V_{max}	280	knots
Wing span	b	32.17	ft
Wing area	S	181.0	ft^2
Rotor radius	R	12.50	ft
Rotor solidity	σ	0.103	n.d.
Rotor Lock number	γ	3.768	n.d.
Rotor rotating speed	Ω	601[a]	rpm

[a] Reduced to 480.8 rpm in airplane mode.

where $\mathbf{x}$ is the vector of the kinematic unknowns, $\mathbf{p}$ is the vector of the momentum unknowns, λ collects the algebraic Lagrangian multipliers, $\mathbf{M}$ is a configuration- (and possibly time-)dependent inertia matrix, vectors $\mathbf{f}_i$ and $\mathbf{f}_e$ contain generalized internal and external forces, $\boldsymbol{\phi}(\mathbf{x})$ is the vector of the algebraic equations that express kinematic holonomic constraints, and $\boldsymbol{\phi}_{/\mathbf{x}}$ is the Jacobian matrix of the constraints with respect to the kinematic unknowns.

Each node instantiates the corresponding balance equations (1b). Nodes with associated inertia properties also instantiate the related momenta definitions (1a).

Elements are responsible for the contributions to the balance equations through visco-elastic, internal forces $\mathbf{f}_i$, possibly state-dependent external force fields $\mathbf{f}_e$ (e.g., aerodynamic forces), and reaction forces $\mathbf{f}_c = \boldsymbol{\phi}_{/\mathbf{x}}^{T}\lambda$, introduced using the Lagrange multipliers λ and the Jacobian matrix of the algebraic constraint equations in Eq. (1c).

The DAE system can be integrated using different A/L stable integration methods, among which is an original multistep one with tunable algorithmic dissipation, specifically designed for the class of problems usually solved with MBDyn [36].

The nodes that describe the kinematics of the structural problem can be connected either by elastic/viscoelastic internal forces (namely lumped structural components [37], beams [38,39], shells [40], Component Mode Synthesis (CMS) elements [41]) expressed by $\mathbf{f}_i$, with a variety of viscoelastic constitutive laws, or by the kinematic constraints of Equation (1c).

Simple aerodynamics can be modeled by built-in elements that exploit the 2D strip theory model by look-up tables of the aerodynamic coefficients and classical rotor inflow models based on momentum theory.

2.3. Aeroelastic coupling

Communications between the two solvers are managed by preCICE (Precise Code Interaction Coupling Environment) [26], a coupling library for partitioned multi-physics simulations, originally developed for fluid-structure interaction and conjugate heat transfer simulations. The interface between structural and aerodynamic grids is obtained as a weighted average of the distance between the nodes of the two grids and is used for motion interpolation and consistent force and moment reduction. The details about the coupling between DUST and MBDyn, with the relative validations, are described in [27].

3. Tiltrotor model setup

A detailed tiltrotor model, representative of the Bell XV-15 research aircraft with Advanced Technology Blades (ATBs) [42], has been built in DUST-MBDyn using data published by Acree in Ref. [28]. The general characteristics are summarized in Table 1.

The model, illustrated in Fig. 1, includes the two proprotors, the wing, the nacelles, and the empennages. The dynamic model setup and the validation of the different sub-components are presented in the next sections. Different levels of complexity are considered in the following,

Table 2
Proprotor frequencies in a vacuum. Comparison between CAMRAD-JA and MBDyn.

	CAMRAD-JA (80% rpm, $\theta_{0_{75}} = 40°$)			MBDyn (80% rpm, $\theta_{0_{75}} = 40°$)		
Mode	Collective	Regressive	Progressive	Collective	Regressive	Progressive
Gimbal, Hz	–	0.24	16.27	–	0.05	16.25
First Lag, Hz	10.19	2.42	18.45	10.53	2.83	19.10
First Flap, Hz	15.94	22.85	38.88	15.35	22.57	38.83
First Torsion, Hz	28.87	20.44	36.47	30.75	18.74	35.72

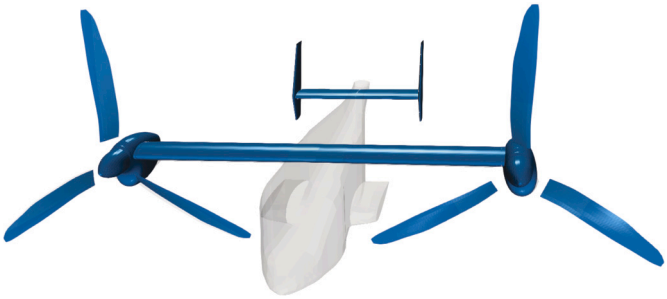

Fig. 1. XV-15 tiltrotor model in DUST-MBDyn.

to highlight the role of interactional aerodynamics on aeroelastic analyses.

3.1. Proprotor

The XV-15 proprotor model with ATBs is made up of composite blades. The rotor is stiff-in-plane with a gimballed hub. The main rotor data are taken from the CAMRAD-JA model presented in [28]. The flexible blades were modeled using the nonlinear beam elements of MBDyn [38], including the control chain.

Two different models are considered for blade aerodynamics. The low-fidelity model is based on the 2D blade element momentum theory, available in MBDyn. Rotor aerodynamic forces are calculated using two-dimensional airfoil characteristics provided by Acree in Ref. [28]. The induced velocity is included as well through a Glauert model [43]. Empirical corrections to account for nonideal induced power losses and a linear variation of the induced velocity over the rotor disk due to nonaxial flow are defined in Ref. [28]. The mid-fidelity aerodynamic model is realized in DUST. Each blade is modeled with a lifting line component. Both low- and mid-fidelity aerodynamic models incorporate viscous and compressibility effects by means of the aerodynamic airfoil table `.c81`, in which lift, drag, and pitching moment coefficients are tabulated versus the angle of attack, covering the entire $\pm 180°$ range, and several Mach numbers ranging from 0 to 1.

Validation of the dynamic behavior of the isolated rotor in a vacuum is accomplished through the Campbell diagrams. These diagrams track the rotational frequency of each mode shape against the rotor speed. To generate the Campbell diagrams, several rotor speeds were considered, and the corresponding eigenvalues and eigenvectors were calculated using the eigenanalysis procedure available in MBDyn [44]. The outcomes are presented in Figs. 2(a) and 2(b), representing the collective and cyclic modes, respectively, for a collective pitch angle of 40°.

Table 2 provides a comparison between the frequencies obtained in CAMRAD-JA and MBDyn in airplane mode. The results show good agreement for both collective and cyclic modes, with only slight differences between the two models. However, the most notable disparity between the two models is observed in the first torsion mode. The difference can be attributed to the fact that the CAMRAD-JA model uses a conventional helicopter-like control chain with a single control path, whereas the MBDyn model incorporates the real dual load path to model the control chain. In the following, the results obtained from the low-fidelity MBDyn model are compared with the mid-fidelity DUST-MBDyn model and with the experimental results of OARF [45].

Fig. 3 shows the comparison between the different aerodynamic models employed together with the experimental results in terms of rotor thrust coefficient (C_T/σ) with reference to the collective pitch angle (see Fig. 3(a)). The figure of merit (FM) is shown in Fig. 3(b). The latter is defined as the ratio of the minimum possible power to flight (i.e. the induced power) to the total power, which also includes the profile power (see Ref. [46], Chapter 3). The performance curves obtained with the coupled DUST-MBDyn models quite well resume the behavior of the experimental data in the entire range of collective pitch angles tested. In particular, the model can correctly capture the rotor stall that begins to occur for a collective pitch angle greater than 15°. In contrast, the MBDyn model is not able to correctly capture hover performances: in particular, the slope of the $C_T/\sigma - \theta_0$ curve is steeper compared to the experimental results and the numerical results obtained with DUST-MBDyn, and no stall is predicted. For a more detailed validation of the DUST-MBDyn proprotor model, the interested reader is referred to [47].

3.2. Airframe

The airframe model encompasses the main wing, nacelles, horizontal and vertical tailplanes, as well as the control surfaces. The aerodynamic surface of the fuselage is not modeled in DUST at this stage, to reduce the computational burden of the coupled analyses, although its contribution is recovered through the aerodynamic lookup tables provided by Ferguson in [48].

The multibody model is composed of 14 rigid bodies representing the different parts of the tiltrotor. Each body includes mass and inertia properties located at the center of mass of each corresponding component. Inertial data are taken from the XV-15 finite element stick model provided by Acree et al. in Ref. [49].

The airframe includes all control surfaces, namely two flaps, two flaperons, an elevator, and two rudders. All movables, except for the flaperons, are modeled as rigid bodies with associated polar inertia, attached to the fixed part through a statically determined constraint modeled as a combination of a spherical joint and an inline joint. The deflection of each control surface is achieved by directly imposing the rotation of the hinge axis in MBDyn. The deformation of the aerodynamic mesh follows the rotation of the structural nodes associated with that axis, as presented in Ref. [50].

A more detailed model has been implemented for the flaperons, including the actuation system together with the corresponding servovalve dynamics [51], with the possibility of introducing the elasticity of the movable surface itself. In this way, it is possible to monitor the loads on the actuators during the maneuver, simulate the control deflection with more realistic dynamics, and evaluate the impact of the flexibility of the surface on the load distribution. In the absence of detailed data concerning the actuation mechanism, a generic design procedure is followed. The constraints to be met are the position of the hinge axis, placed at 75% of the chord, and the max deflection of 47°. A value of −25° is assumed as the maximum upward deflection. The actuation mechanism is characterized by three points: the hinge point and the two actuator heads (see Fig. 4(a)). The left actuator head is connected to the fixed wing. The right actuator head, on the other hand, lies on the flaperon and slides along a circular trajectory, represented by the red dashed line in Fig. 4(a). The radius has been designed to ensure the accommodation of the system within the wing section. The actuator is

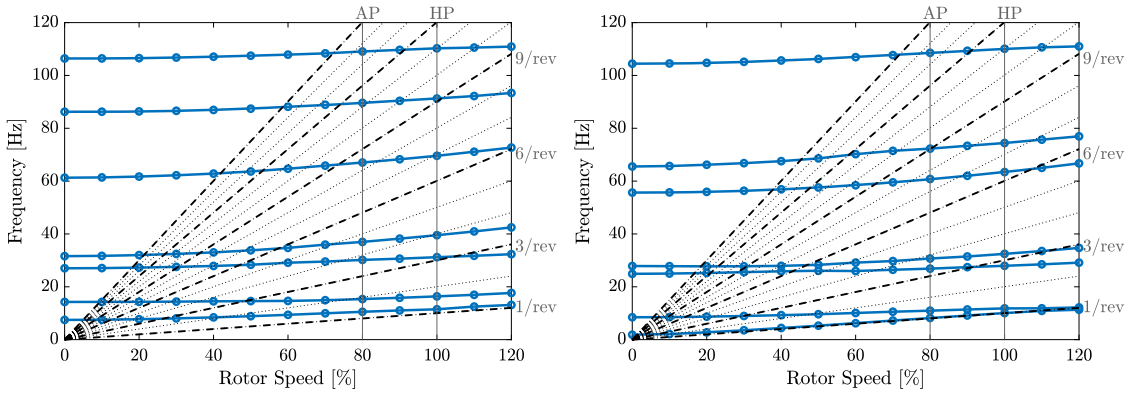

(a) Collective Modes. (b) Cyclic modes.

Fig. 2. Proprotor Campbell diagrams in a vacuum – $\theta_{0_{75}} = 40°$.

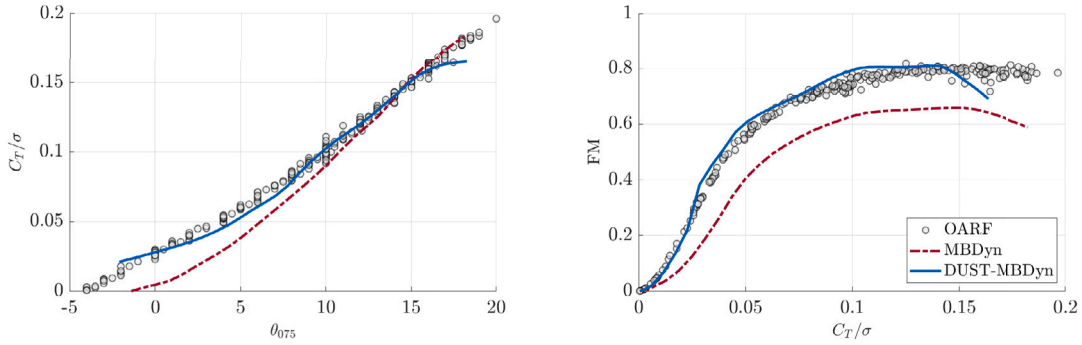

(a) C_T/σ vs $\theta_{0_{75}}$. (b) FM vs C_T/σ.

Fig. 3. Proprotor performances in hover.

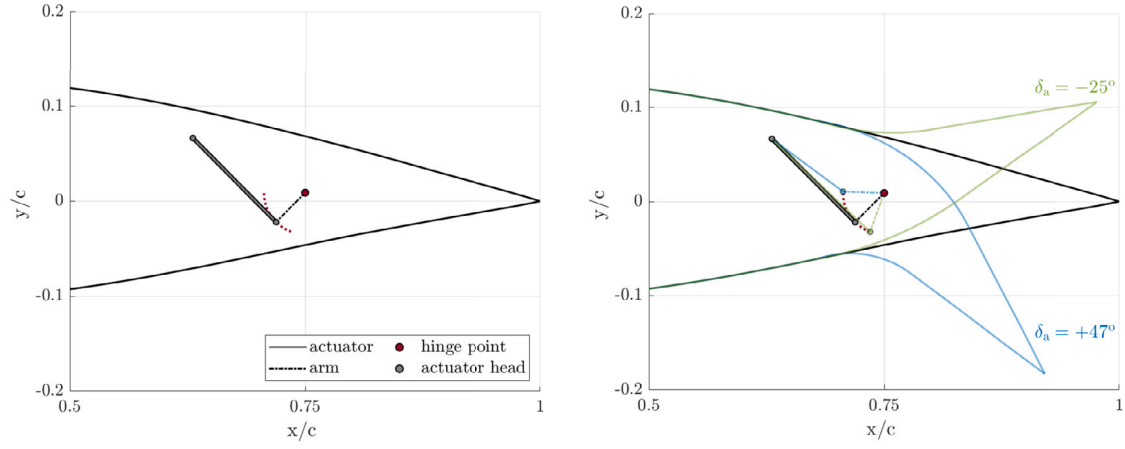

(a) Undeflected configuration. (b) Deflected configuration.

Fig. 4. Flaperon actuation system. (For interpretation of the colors in the figure(s), the reader is referred to the web version of this article.)

perpendicular to the radius when the flaperon deflection is null. Considering the space constraints, an actuator length of 200 mm and a radius of 70 mm have been chosen. The relative displacement of the actuator and the corresponding flaperon deflection is shown in Fig. 4(b).

The actuator elongation, see Fig. 5(a), has a fairly linear trend with respect to the flaperon deflection. Nonlinear effects are only evident at high-deflection angles. The travel arm shows instead a nonlinear trend, depicted in Fig. 5(b).

The actuator dynamic compliance is described by Eq. (2). The pilot's input is filtered by a second-order low-pass Butterworth filter with a cut-off frequency of 7 Hz, representing the servo-valve dynamics of the actuator. The actuator force F_{act} is reconstructed using a visco-elastic constitutive law, namely

$$F_{\text{act}} = -K_a \Delta L_f - C_a \Delta \dot{L}_f, \tag{2}$$

where ΔL_f is the filtered actuator length variation and K_a and C_a are the corresponding actuator stiffness and damping characteristics. Those are inspired by data taken from similar aircraft, mounting 3 actuators on each control surface. An equivalent linear stiffness K_a of $2.8 \times 10^7\,\text{N m}^{-1}$ has been taken into account, to provide a robust con-

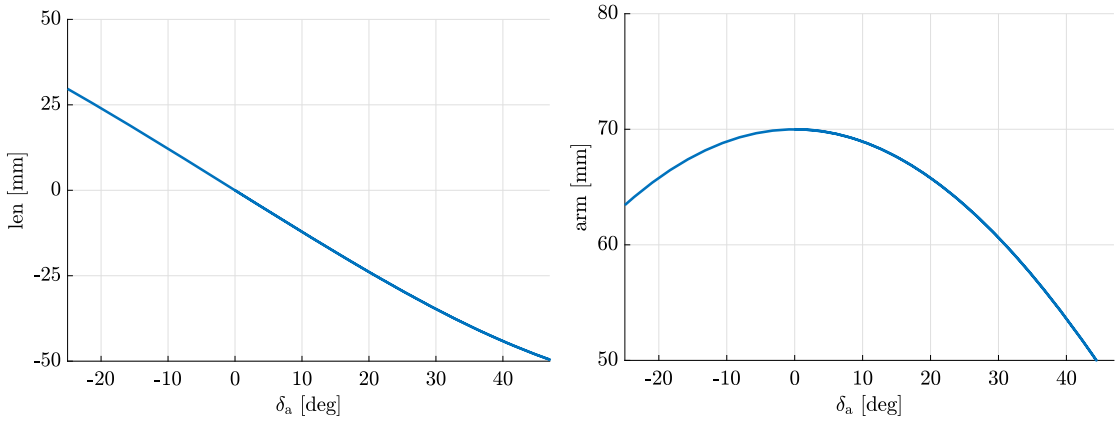

(a) Actuators length. (b) Travel arm length.

Fig. 5. Flaperon actuation system kinematics.

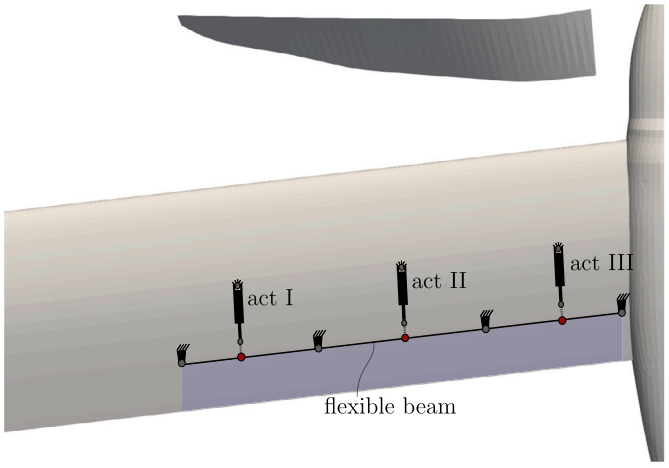

Fig. 6. Flaperon actuation mechanism scheme, right-wing.

Table 3
Estimated XV-15 flaperon structural properties.

EA	EJ_{xx}	EJ_{zz}	GJ
N	$\mathrm{N\,m^2}$	$\mathrm{N\,m^2}$	$\mathrm{N\,m^2}$
$8.39 \cdot 10^7$	$1.63 \cdot 10^5$	$1.51 \cdot 10^6$	$2.62 \cdot 10^4$

nection with the fixed wing and to avoid aeroelastic instabilities due to the control surface. The actuator damping C_a has been added to eliminate high-frequency oscillations on the time responses.

The XV-15 flaperon, shown in Fig. 6, is modeled in MBDyn as a flexible `beam3` element, as done for the rotor blades. 3 flexible beams are anchored to the main wing component through four spherical hinges that allow the rotation of the control surface about the hinge axis. The flaperon structural properties, summarized in Table 3, have been estimated starting from the wing structural data provided by [28], and considering a simple semi-monocoque idealization of the flaperon cross-section (see Ref. [52], Chapter 20). Technical details can be found in Ref. [53].

3.3. Airframe aerodynamic validation

To assess the capability of DUST to capture the complex three-dimensional aerodynamics due to the presence of the nacelle in the wing tip region, the isolated wing-pylon sub-system is here considered.

The aerodynamic coefficients of the wing-pylon system as a function of the angle of attack are known from [48]. To carry out a full aerodynamic validation, a high-fidelity CFD model has been built in order to provide more comparative results. The numerical model includes the flaperons as well. The selected CFD solver is SU2 [54], an open-source software freely available and licensed under the GNU Lesser General Public License.

The grid used in this work, see Fig. 7(a), is a mixed-element grid composed of 19M total elements. The mesh is composed of tetrahedra, prisms, and pyramids around a surface that has been discretized using triangles and quads. For the simulation, the right semi-model was modeled by imposing the symmetry boundary condition on the longitudinal plane. The far-field boundary is located approximately more than 25 body span lengths away from the aircraft, with the first cell thickness in the boundary layer region to allow for $y^+ \approx 1$. The level of the volume grid refinement is managed through two sub-zones, encapsulating wing and nacelle respectively. A Jameson-Schmidt-Turkel (JST)-centered spatial discretization is used to calculate convective fluxes in the RANS computation. Turbulent variables for the SST models are convected using a first-order scalar upwind method, and the viscous fluxes are calculated using the corrected average-gradient method. Implicit, local time stepping is used to converge the problem to the steady-state solution, and the linear system is solved using the iterative BCGSTAB method with a maximum error tolerance of $\mathcal{O}(10^{-4})$.

The DUST numerical model of the wing-pylon system is modeled as surface panels (SP). Fig. 7(b) illustrates the half-right part of the DUST aerodynamic mesh. To model the flaperon, the DUST hinge component [27] is exploited, obtaining a deflected wing region and maintaining the continuity of the mesh. Regarding the mesh discretization in the chord section, a double refinement is employed both in the leading edge and in the hinge axis location.

The wing-pylon aerodynamic system is tested by comparing high-fidelity SU2 results with the DUST mid-fidelity results. Considering the cruise speed condition at Mach = 0.4, the aerodynamic coefficients between -6° and $+8^\circ$ degrees of angle of attack (AoA°) are computed, for three different flaperon deflections (δ_a), namely $\delta_a = 0^\circ$, 10°, and 20°.

Figs. 8(a) and 8(b) show the aerodynamic loads in terms of lift and drag coefficients. In the linear region, the lift coefficient obtained with DUST shows a good agreement with SU2 and with experimental data provided by Ferguson [48]. The nonlinear effects on the lift curve related to stall are not captured by DUST, as can be expected considering the inviscid flow assumptions of the numerical method. The good agreement in the drag coefficient between the SU2 simulations and the experimental data available for δ_a equal to 0° confirms the goodness of the high-fidelity model built to make comparisons with DUST. Since the parasite drag is not modeled by the mid-fidelity solver, there is an offset between the DUST and SU2 drag coefficient curves. On the other hand, since the induced drag generated by the wing tip vortices is al-

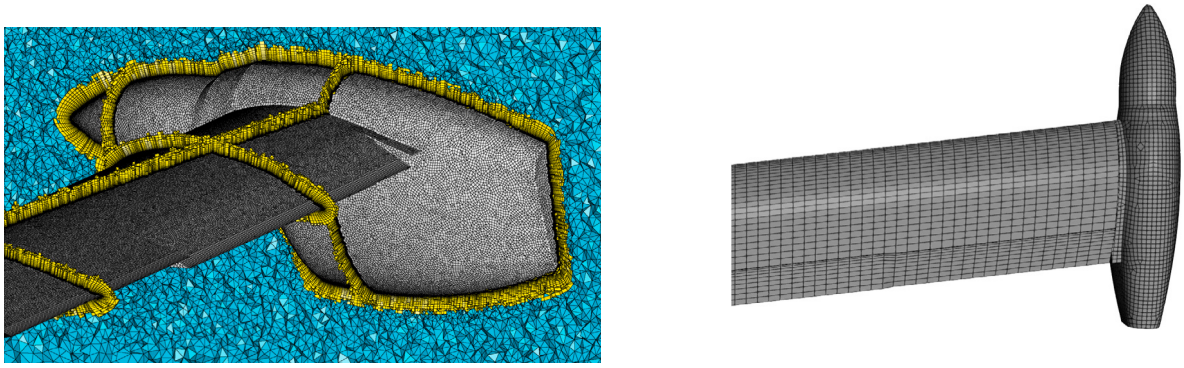

(a) CFD grid detail. (b) DUST surface half mesh.

Fig. 7. Aerodynamic mesh for the XV-15 wing-pylon system.

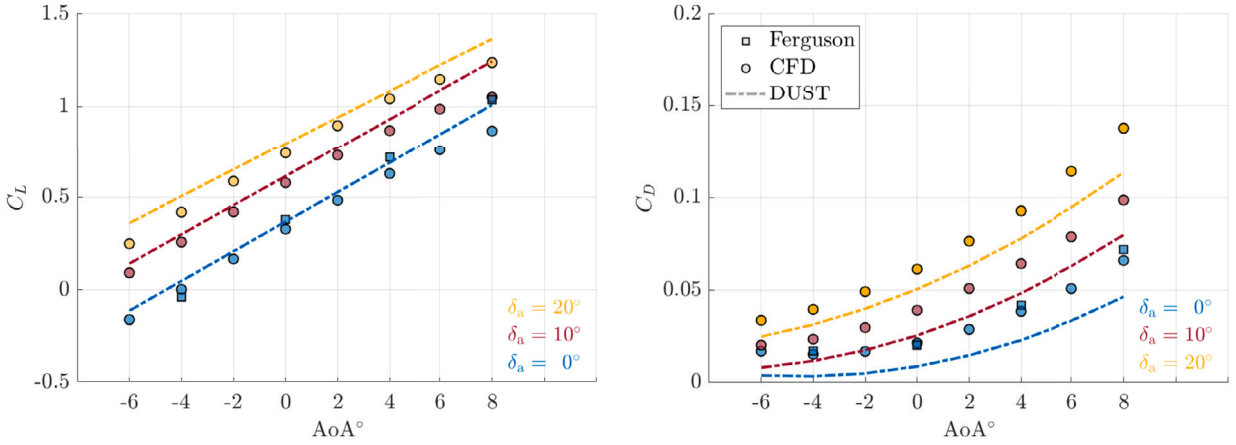

(a) Lift coefficient vs angle of attack. (b) Drag coefficient vs angle of attack.

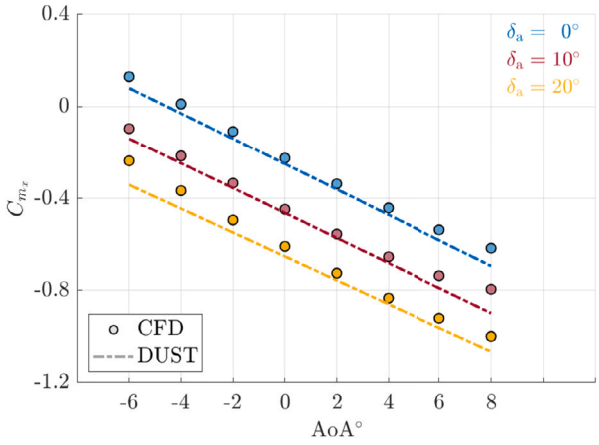

(c) Roll moment coefficient vs angle of attack.

Fig. 8. Wing-pylon system aerodynamic performances comparison between SU2 and DUST.

most well represented, all the curves show good trends with reference to the AoA° and δ_a.

In terms of global performance indexes, it is interesting to analyze the roll moment generated about the longitudinal axis of the aircraft, due to a flaperon deflection. Fig. 8(c) depicts the moment coefficient about the longitudinal axis considering the right semi-model as a function of the angle of attack for three different flaperon deflections. These results confirm a good correlation between SU2 and DUST encouraging the use of the mid-fidelity aerodynamic model to simulate roll maneuvers.

A more detailed view of the load distribution on the wing-nacelle system is given by the comparison of the pressure coefficient shown in Fig. 9, evaluated at AoA° = 0° and $\delta_a = 0°$. Indeed, DUST results are consistent with those obtained by the CFD model. This is valid as long as the angle of attack is small and there are no separation zones. Moreover, the comparison highlights a good correlation in the wingtip area, where the nacelle is installed, which is essential for the correct design of the wing control surfaces, located in the same region.

Finally, Fig. 10 shows the pressure coefficient extracted at the six spanwise stations illustrated in Fig. 9. The pressure coefficient along the

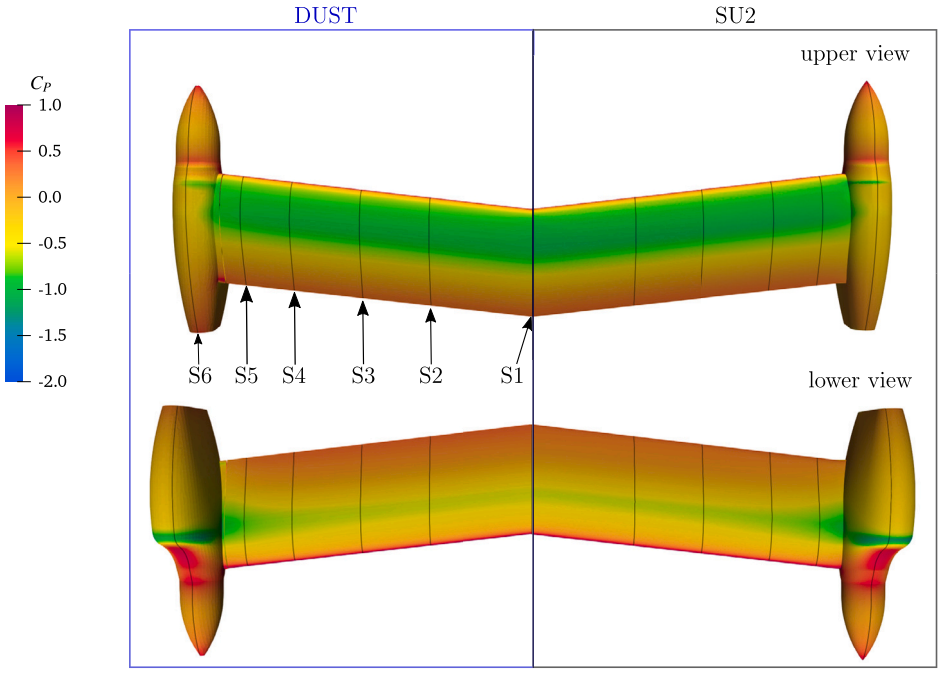

Fig. 9. Pressure coefficient comparison between SU2 and DUST.

wing sections (from Fig. 10(a) to Fig. 10(e)) confirms the DUST capability to well capture the effect of the nacelle on the wing aerodynamic loads. Moreover, Fig. 10(f) shows good consistency even on the bluff body of the nacelle. Of course, this does not mean that DUST captures the entire aerodynamic load that is also characterized by the presence of large flow separation behind the nacelle, with a significant drag component due to the viscous effects, not modeled by the mid-fidelity tool.

4. Proposed analyses

The analyses presented in this section include static and dynamic load predictions. An extended validation of the static loads when considering trim conditions in airplane mode is provided in the following, with a reference model based on wind tunnel tests and flight test data. Unfortunately, no comparative data are available in the literature for the validation of dynamic loads during the transient maneuvers. However, the accuracy and capability of the DUST aerodynamic solver to capture unsteady aerodynamic phenomena have been extensively tested and validated for several wing-rotor configurations, as reported in Ref. [53].

4.1. Trim

The purpose of this analysis is to demonstrate the additional information that can be assessed with the proposed approach in a trim problem. In particular, the novelties are not related to the static trim results but to those concerning the evaluation of periodic unsteady loads, relevant for vibratory levels, ride qualities, and fatigue assessments. Thanks to DUST's aerodynamics, these loads include the contribution related to the interactional aerodynamics and do not require the user to choose any corrective factor.

For a symmetric flight condition in airplane mode, the trim problem consists of computing the elevator deflection δ, the aircraft pitch angle θ, and the collective pitch angle θ_0 such that the tiltrotor reaches the equilibrium point in steady level flight. Flight speed and altitude are imposed. However, since the parasite drag is not captured in DUST, the equilibrium condition in the longitudinal direction is not considered at this stage. The collective pitch angle θ_0 is then computed to maintain a constant rotor speed ω^{des} by imposing a desired torque value, provided in Ref. [55], decoupling the rotor and the airframe block. The block scheme of the tiltrotor trim procedure is represented in Fig. 11, where the superscript $^{\text{eval}}$ indicates the quantities evaluated during the simulation.

For the airframe part, the problem reduces to finding the elevator deflection and pitch angle that guarantee the global equilibrium in the vertical direction and about the pitch axis. The simulation is initialized by setting an initial guess for the elevator and the pitch angle. A total joint is initially defined at the aircraft's center of mass to constrain the rigid-body motion. Then, a Proportional-Integral (PI) regulator is introduced in the simulation with the aim of bringing to zero the vertical reaction force T_z^{des} and the pitching moment M_y^{des} of the total joint, by computing δ and θ. Only after the computation of the trim point, the total joint is removed.

Since the objective of the controller is to bring the reaction forces to zero, minimizing the error ϵ, the most significant contributions are due to the integral part, to eliminate steady-state error. The proportional-integral gains are designed following the procedure presented by Mattaboni et al. in Ref. [11], minimizing the transients to reach the trim condition without exciting the aircraft's structural dynamics.

For trim analysis, two aerodynamic models are considered for proprotors. In particular, the Blade Element Momentum Theory implemented in MBDyn is used for the first model, while lifting lines implemented in DUST are used for the second model, as discussed in Sec. 3.1. The airframe aerodynamics are modeled with surface panels in DUST, following the results obtained in Sec. 3.2. For the sake of brevity, the first model will be referred to us *Model A* while the second *Model B*. The purpose of this dual modeling approach is to emphasize the importance of having an aerodynamic model that allows the interactions between the different parts to be included, even at a preliminary design stage, especially when dealing with a complex aircraft such as a tiltrotor or, more generally, with a multi-rotor configuration.

4.2. Roll maneuver

After the computation of the trim point, the aileron maneuver is considered to investigate the aircraft's response to roll dynamics. The maneuver consists of deflecting the flaperons of $\pm 10^\circ$ starting from a trimmed condition in steady level flight at the cruise speed

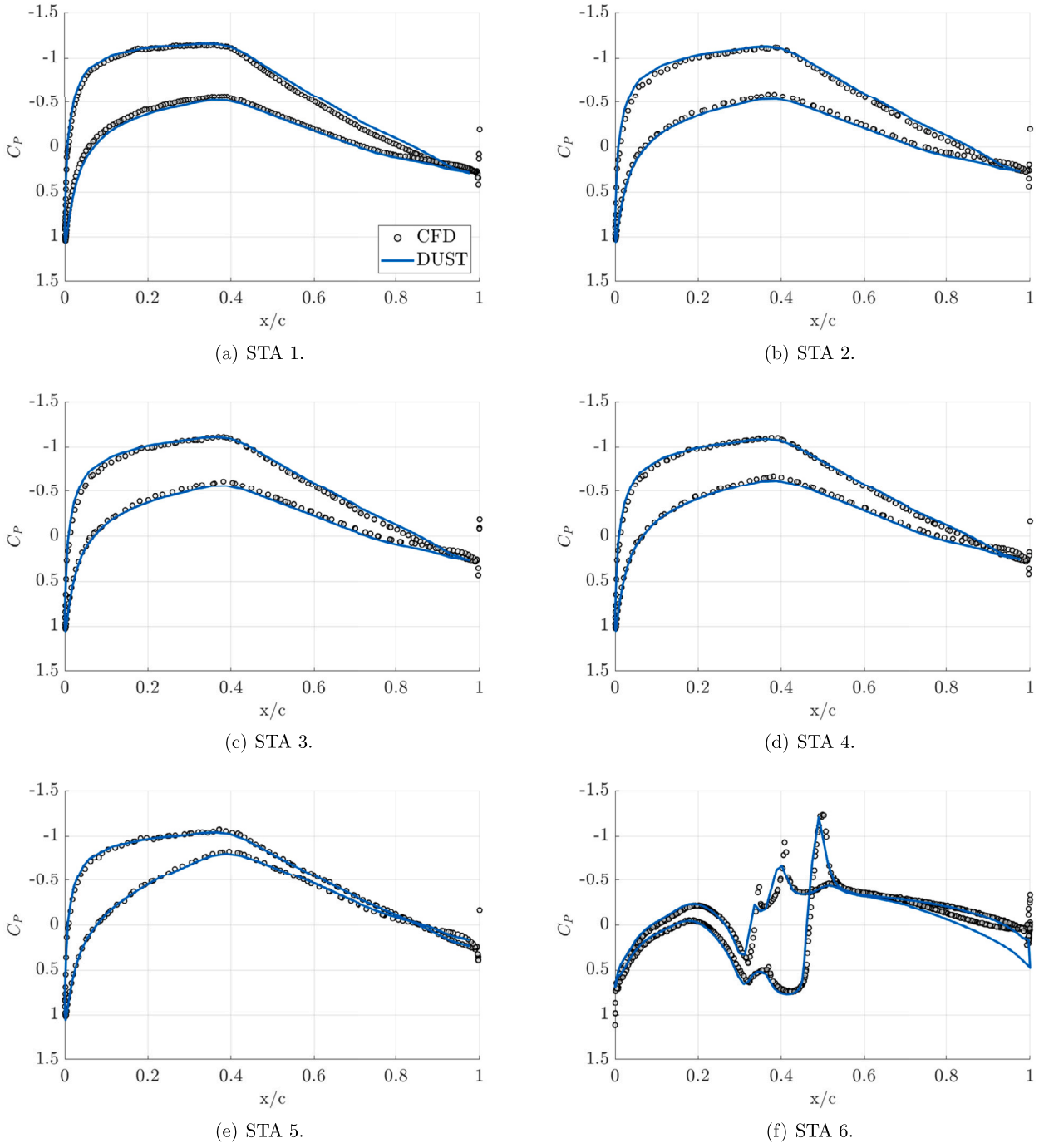

(a) STA 1. (b) STA 2.

(c) STA 3. (d) STA 4.

(e) STA 5. (f) STA 6.

Fig. 10. Pressure coefficient distribution at the six span stations considered, AoA° = 0° and $\delta_a = 0°$.

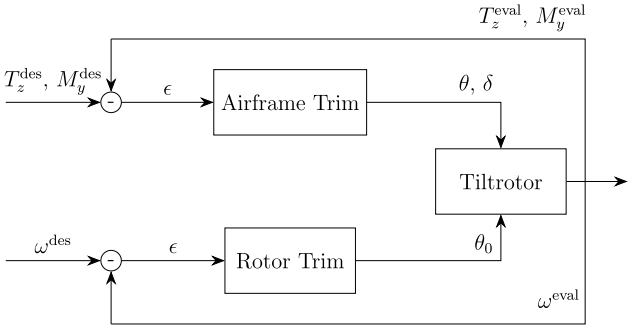

Fig. 11. Tiltrotor trim scheme.

(U_∞ = 260 knots) with the aircraft free to rotate about its longitudinal axis. The maneuver is accomplished when a bank angle of 30° is reached.

From the viewpoint of the simulation procedure, once the trim condition has been identified, a new simulation is started by imposing the trim values as initial conditions. Once the transient aerodynamic effects caused by the initial start-up are exhausted (a time of 0.5 s corresponding to 4 rotor revolutions is considered in the present work), the aircraft is allowed to roll about its longitudinal axis and the aileron command is imposed. To control the deflection of each flaperon, the elongation of the actuators is imposed through the kinematic relationship obtained in Fig. 5, which is subsequently filtered to reproduce the dynamic response of the system.

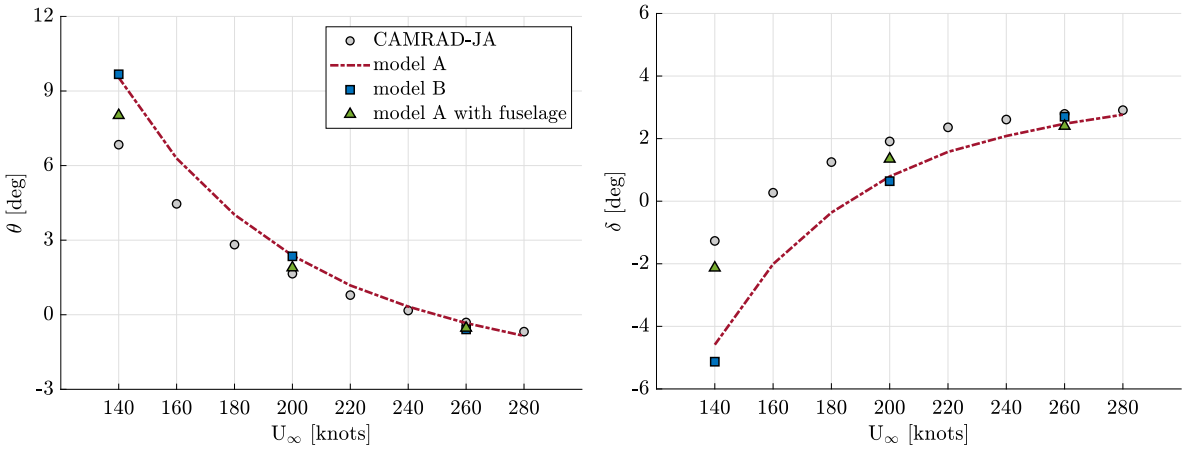

(a) Pitch attitude θ. (b) Elevator deflection δ.

Fig. 12. Airframe trim variables with reference to the flight speed.

Table 4
Model configurations used for the roll maneuver.

Configuration	Rotor Speed [RPM]	Gimbal	Rotor wake	Elastic Flaperons
I	0	lock	NO	NO
II (*Model A*)	480	unlock	NO	NO
III (*Model B*)	480	unlock	YES	NO
IV	480	unlock	YES	YES

Several models of increasing complexity have been taken into account to demonstrate the capabilities of the coupled tool in predicting tiltrotor performance indexes and aeroelastic loads.

In particular, by exploiting the incremental configurations in terms of model complexity reported in Table 4, the following aspects are intended to be highlighted:

- **Impact of rotor dynamics**: comparison between configurations I and II. Configuration I does not involve rotor rotation and the associated rotor dynamics, although rotor mass and inertia properties are taken into account. Configuration II corresponds to *Model A* where the rotor dynamics are considered, together with the basic aerodynamics based on BEMT.
- **Impact of rotor aerodynamics interaction**: comparison between configurations II and III. Configuration III, corresponding to *Model B*, replaces MBDyn rotor aerodynamics with DUST aerodynamics, thus introducing the component of interactional aerodynamics in the model through the rotor wake.
- **Impact of flaperon elasticity**: comparison between configurations III and IV. Configuration IV includes the flaperon elasticity added by flexible beams on the movables, as presented in Sec. 3.2. This last analysis aims to highlight the repartitioning of loads on actuators when considering the flexibility of the control surface.

5. Results and discussion

5.1. Trim

The resulting airframe trim variables with reference to the flight speed are shown in Fig. 12, compared to similar results obtained in CAMRAD-JA [55]. The last is considered a suitable reference model since it is based on the aerodynamic characteristics provided by Ferguson in Ref. [56], obtained from wind tunnel tests and flight test data. The dashed red curve refers to the model with hybrid aerodynamics, i.e. *Model A*, while the blue square markers refer to the model with full DUST aerodynamics, that is *Model B*. Both models provide similar results to the CAMRAD-JA reference model. At low speeds, on the other hand, it was found a marked deviation from the reference trim curves, with noticeable differences in the elevator angle up to 3.5°. Upon investigation, it was found that the drift was caused by the absence of the fuselage aerodynamics. To verify this hypothesis, an aerobody element representing the static aerodynamics of the fuselage was introduced in MBDyn, based on the aerodynamic lookup tables provided in Ref. [56]. In Fig. 12, the results obtained with the updated *Model A*, which now includes the aerodynamics of the fuselage, are shown for three characteristic speeds. The contribution of the fuselage allows us to reduce the difference with the reference trim data, especially at low-speed flight conditions, where the corresponding pitching moment due to the fuselage is not negligible.

As expected, there are no significant differences between *Model A* and *Model B* on the static trim curves. Indeed, both the pitch attitude and the elevator angle in trim conditions only depend on the static load components. These results are not largely affected by the presence of the rotor wake, responsible for the generation of periodic loads on the aircraft. On the other hand, the correct evaluation of periodic trim loads allows us to determine the vibratory level of the aircraft as well as provides information for fatigue loads.

To highlight the differences between the two models, the aerodynamic loads on the wing and horizontal tail plane along a complete rotor revolution are considered in the following, for a steady level flight condition at 260 knots.

Results in terms of sectional normal forces on the right semi-span wing and horizontal tail during a proprotor revolution are shown in Fig. 13. The horizontal axis depicts the non-dimensional spanwise coordinate, namely $2y/b$, where b is the total span of the wing. For the horizontal tailplane, the total span is indicated as b_t.

Periodic loads are observed as a function of the rotor azimuth angle, caused by the interaction of the rotor's wake with the wing and the empennages. Three distinct regions can be identified where the wake of each of the three blades passes through. As a result, the loads on the wing and on the empennages are not constant but rather exhibit periodic variations with the rotor speed. The first peak for the wing is observed at $\psi = 80°$ while the horizontal tailplane, being further back, perceives it at approximately $\psi = 100°$. These results are related to the evolution of the rotor wake calculated by DUST. Indeed, Fig. 14 shows the position of the vortical particles and their interaction with the wing and the empennages for $\psi = 80°$ and $\psi = 100°$. At $\psi = 80°$, the wake of the third blade impacts the wing and modifies its load distribution, while the horizontal tail plane remains unaffected. However, as the wake proceeds downstream ($\psi = 100°$), the particles released by the first blade impact the horizontal tailplane. The particles are partially canalized between the horizontal tail and the vertical plane, generat-

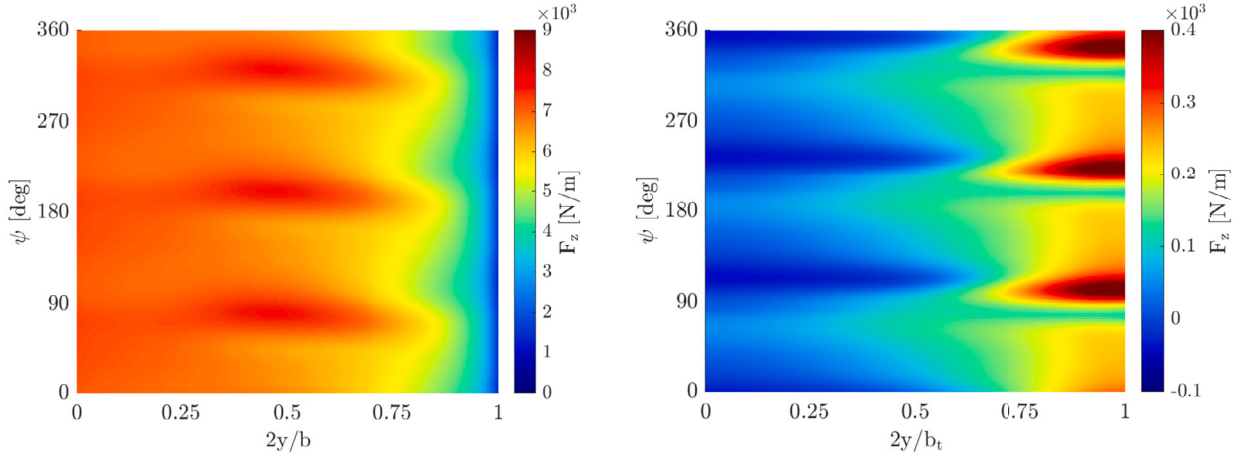

(a) Wing. (b) Horizontal tail.

Fig. 13. Comparison of the contours of the sectional normal force on the right wing and horizontal tail during a proprotor revolution. *Model B*, $U_\infty = 260$ knots.

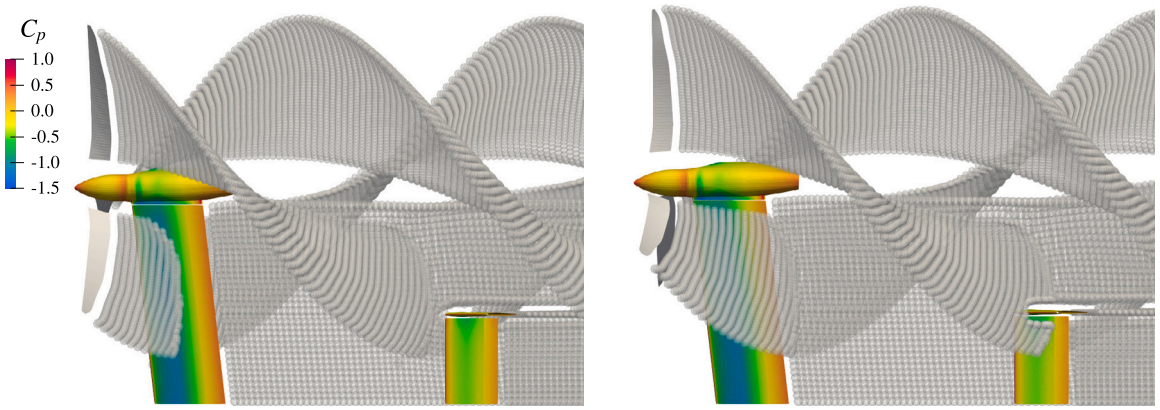

(a) $\psi = 80°$. (b) $\psi = 100°$.

Fig. 14. Comparison of wake structure for different rotor azimuth ψ, $U_\infty = 260$ knots.

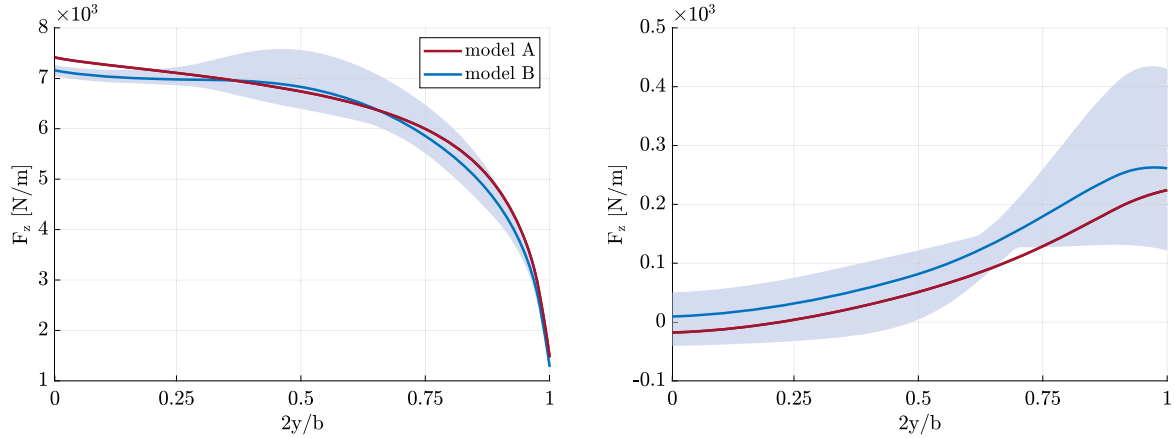

(a) Right wing. (b) Right horizontal tail.

Fig. 15. Comparison of the sectional normal force, $U_\infty = 260$ knots; the variation of the load around the mean value is represented by a shaded region.

ing a higher velocity region and therefore a static pressure reduction, which is responsible for the increase in the sectional load in that area.

Sectional loads along the spanwise for the wing and horizontal tail are shown in Fig. 15. The variation of the load around the mean value (solid blue line) for *Model B* is represented by the shaded blue region. For the main wing, the difference between the mean value of the two models is relatively small, and the greatest variation is obtained at $2y/b = 0.5$, where the most intense vortices released by the rotor pass through. The results shown in Fig. 15(b) for the tail section reveal a difference in the mean values obtained with the two models. Specifically, *Model B* displays a higher mean load on the entire horizontal tailplane. Indeed, the wake from the main rotor impacts the horizon-

tal tail increasing the lift. However, it should be noted that the elevator deflection between the two models is slightly different, and *Model B* returns a smaller value of about 0.25° compared to *Model A*, which also contributes to the higher averaged load. Regarding the variation of the periodic load, the entire surface appears to be affected. In particular, the greatest interaction is observed at the tip of the horizontal tail, where the vertical tail is also attached, in accordance with Fig. 14(b).

To identify a set of relevant loads, three monitor points – illustrated in Fig. 16 – are considered in the following, where internal forces and moments are computed. P_1 and P_2 are located at the root of the wing and horizontal tail plane respectively. P_3 is located at the blade root, for the evaluation of the blade loads in a rotating reference frame.

The first set of loads depicts the out-of-plane bending moment and the in-plane shear force measured on P_1. Similarly, for P_2, the out-of-plane bending moment is evaluated. Flapping and lagging bending moments are computed on P_3. These loads are transmitted from the blade to the yoke and are critical for the rotor structural integrity and aircraft performance.

Figs. 17(a) and 17(b) show respectively the in-plane shear force and the bending moment evaluated during one rotor revolution at P_1. The oscillations evaluated with *Model B* are significant compared to the average values and play a fundamental role in fatigue life and vibratory level of the tiltrotor. The average load, on the other hand, remains similar between the two models.

The out-of-plane bending moment on P_2 shows instead different mean components between *Model A* and *Model B*, due to the different spanwise load distribution shown in Fig. 15(b). Additionally, *Model B* allows us to capture the periodic loads associated with the evolution of the wake impacting on the tail. Fig. 18(b) clearly identifies the harmonic content with reference to rotor multiples of the n/rev, where n is the number of blades, with non-negligible amplitudes up to the $12/rev$.

Similar considerations can be made on the rotor loads. Fig. 19(a) shows the bending moments measured at the blade root. In the following, $M_{z,yoke}$ and $M_{y,yoke}$ respectively indicate the components of the lagwise and flapwise bending moments. To analyze the differences between the two models, the time histories and the corresponding Fast Fourier Transforms (FFT) are shown in Fig. 19.

Once again, the interactional aerodynamics allow capturing the higher harmonic loads, thus providing a more complete data set useful for tiltrotor analysis and design. For instance, when considering the bending moment associated with flapping dynamics ($M_{y,yoke}$), *model B* shows a non-negligible term at $3/rev$, whose amplitude is almost one-third of the first harmonic at $1/rev$.

As a matter of fact, neglecting the aerodynamic interaction between the rotor and the airframe can lead to a loss of information concerning the periodic trim loads that are the main source of vibration phenomena and fatigue life assessment on tiltrotors. Therefore, design guidelines should consider interactional aerodynamics even during the preliminary design phases, to ensure the rotorcraft's structural integrity and comfort for passengers.

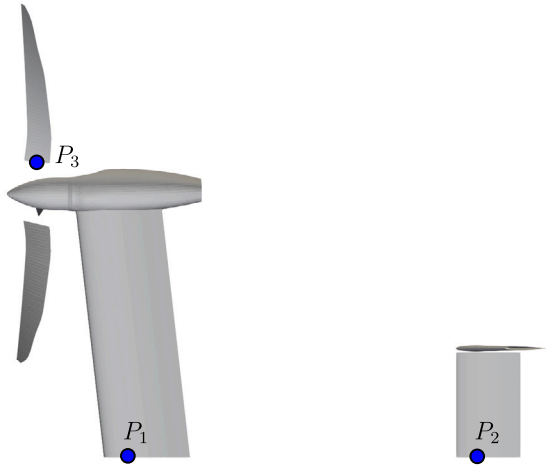

Fig. 16. Monitor points considered on the right half model; top view.

5.2. Roll maneuver

5.2.1. Impact of rotor dynamics

The impact of rotor dynamics on roll maneuver is initially investigated, comparing the results of Configuration I with those obtained with Configuration II. From the perspective of the airframe, the two models coincide in both the MBDyn structural part and the DUST aerodynamic part. However, they differ in rotor modeling. Configuration I only includes the concentrated masses of the blades with null rotor speed and locked gimbal angles. Configuration II corresponds to *Model A* presented in Sec. 5.1, where rotors are modeled with flexible blades and simplified aerodynamics based on BEMT.

During the simulations, the aircraft rolls about the longitudinal axis, positive starboard (right) wing up. Yaw rotation is about the vertical axis, positive nose left while pitch rotation is about the axis normal to the longitudinal plane of symmetry, positive nose up.

Fig. 20(a) shows the evolution of the bank angle ϕ for the two configurations tested. In particular, the figure clearly shows how the rotor dynamics modify the slope of the bank angle curve, reducing roll performance. Specifically, the time-to-bank is decreased by 7% for configuration II when considering a target bank angle of 30°. This

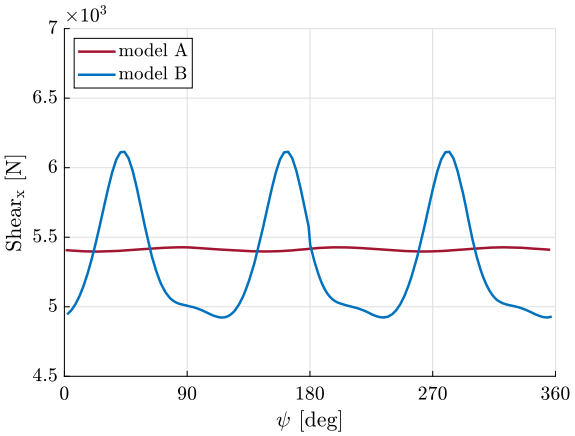

(a) Chordwise shear.

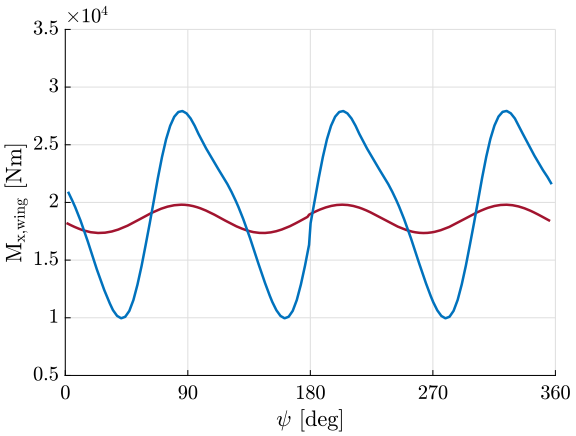

(b) Right wing bending moment.

Fig. 17. Comparison of loads transmitted to the airframe at P_1 for the two different aerodynamic models, $U_\infty = 260$ knots.

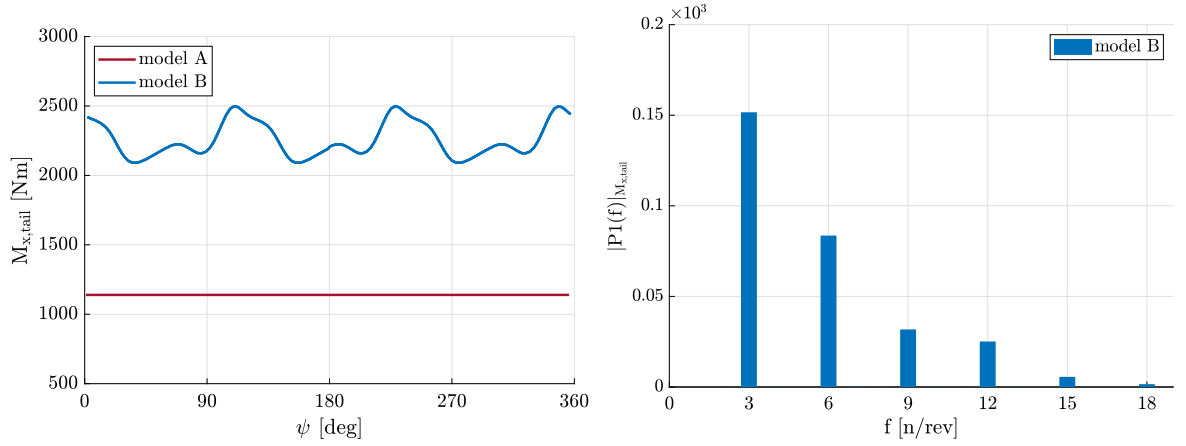

(a) Loads history. (b) FFT.

Fig. 18. Comparison of out-of-plane bending moment transmitted to the horizontal tail root at P_2 for the two different aerodynamic models, $U_\infty = 260$ knots.

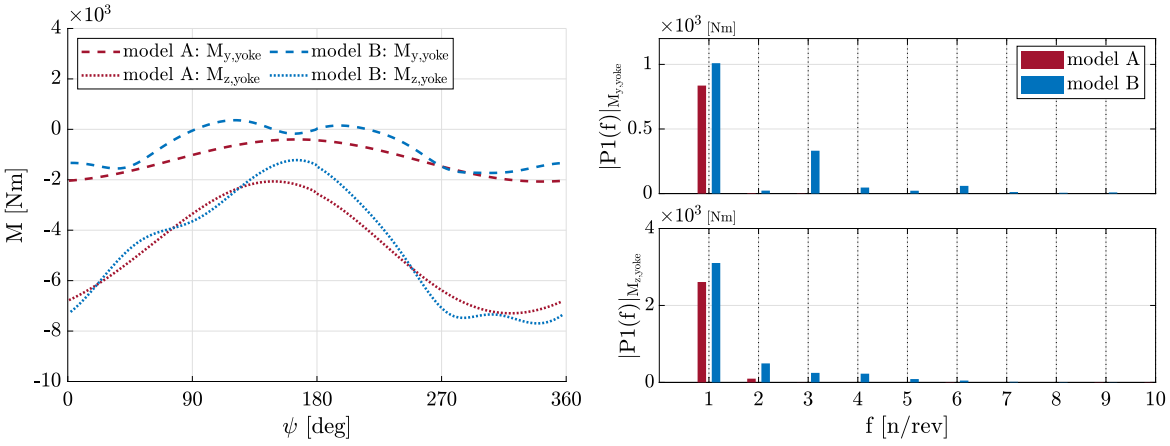

(a) Loads history. (b) FFT.

Fig. 19. Comparison of bending moment loads acting on rotor yoke at P_3 for the two different aerodynamic models, $U_\infty = 260$ knots.

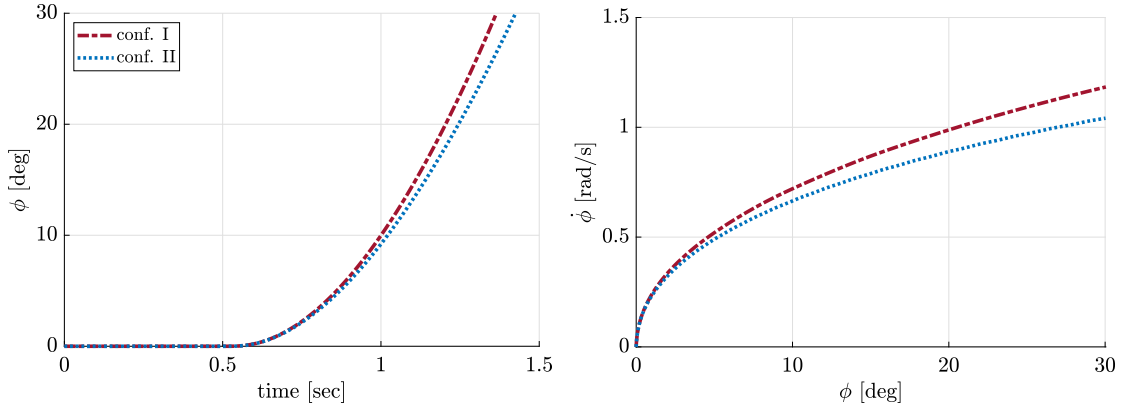

(a) Bank angle ϕ. (b) Roll rate p.

Fig. 20. Comparison of computed bank angle evolution (a), and roll rate evolution (b) for configurations I and II.

is also confirmed by the roll rate ($\dot{\phi}$) depicted in Fig. 20(b). When the right semi-span wing moves upward, the corresponding right rotor flaps downward due to the lower velocity (and reduced lift) of the outer blade. Conversely, the left rotor flaps upward (same mechanism but mirrored). The resulting side forces of the two rotors create a roll moment opposite to the control moment generated by the flaperons, reducing the roll rate.

It must be remarked that the steady level turn also requires control of the aircraft about the yaw axis. In this work, the aircraft is unconstrained only about the longitudinal axis to allow the vehicle to roll. However, it is possible to monitor the yaw moment by measuring the corresponding reaction moment about the aircraft's vertical axis (see Fig. 21). The corresponding forces breakdown related to the wing-pylon, rotors, and tail components are presented as well. Since the yaw

motion is constrained during the simulation, the purpose of these results is to estimate the impact of the different vehicle components on the reaction moment measured about the yaw axis.

The main contribution is related to the adverse yaw moment due to the rotors. The wing-pylon system also introduces a negative component on the yaw moment, which, however, unlike rotors, is quite constant during the maneuver. The tail, on the other hand, turns out to be the only component that generates a proverse yaw. Note that the curves corresponding to the contribution of the tail for the two configurations are overlapped since in both cases there is no rotor wake impacting. The tail contribution results however negligible when compared to the other components. These results demonstrate the importance of the rotor dynamics when evaluating the yaw moment during a roll maneuver, since their relative contribution is the largest.

The dynamic response of the rotors, introduced with configuration II, enables the activation of cyclic flap components as well, generating a tilt of the rotor as a consequence of the roll rate. Indeed, the velocity component associated with the roll motion changes the position of the rotors with respect to the relative flow, moving the rotors away from the axial flow condition as the roll rate increases.

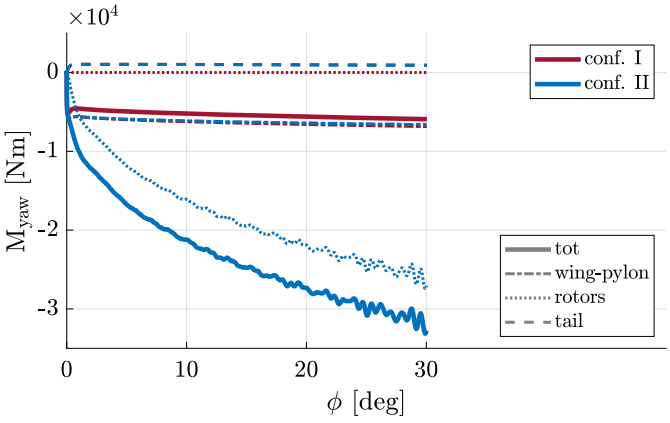

Fig. 21. Comparison of measured yaw moment for configurations I and II.

Fig. 22 is used to compute the relative velocity components during the roll maneuver to estimate the blade's local angle of attack. For the right rotor, the rolling motion reduces the velocity and therefore the local angle of attack at $\psi = 90°$. The opposite effect occurs at $\psi = 270°$ when the blade is in front of the wing. The imbalance introduces an asymmetric load on the rotor disc, generating a flapping motion. As regards the left rotor, the opposite holds true. Eqs. (3a) and (3b) are used to compute the angles of attack for the right and left rotors, considering a radial station located at 75% of the blade. Both equations neglect the induced velocity generated by the rotors, definitely smaller than the freestream velocity in airplane mode.

$$\alpha^r_{R_{75}}(\psi,\dot{\phi}) = \theta_{75} - \tan^{-1}\left(\frac{V^r_{x_2}}{V^r_{y_2}}\right) = \theta_{75} - \tan^{-1}\left(\frac{U_\infty}{\omega R_{75} - \dot{\phi}\left(\frac{b}{2}\sin\psi + R_{75}\right)}\right), \tag{3a}$$

$$\alpha^l_{R_{75}}(\psi,\dot{\phi}) = \theta_{75} - \tan^{-1}\left(\frac{V^l_{x_2}}{V^l_{y_2}}\right) = \theta_{75} - \tan^{-1}\left(\frac{U_\infty}{\omega R_{75} + \dot{\phi}\left(\frac{b}{2}\sin\psi + R_{75}\right)}\right). \tag{3b}$$

Fig. 23(a) shows how the right rotor reduces the local AoA during the roll maneuver, while the AoA on the left rotor increases, leading to the differential thrust shown in Fig. 23(b) and to the insurgence of the adverse yaw moment on the aircraft.

As for the curves related to the wing-pylon and the tail, the models provide identical results since the aerodynamic and structural models are the same, and even though the rotor is present only in configuration II, it does not generate a wake, responsible for aerodynamic interactions with other components.

An adverse yaw moment is also generated by the wing-pylon system. Indeed, the right-wing moves upward providing a downward component of velocity that reduces the effective angle of attack and causes the lift vector to tilt backward. The opposite is true for the left side.

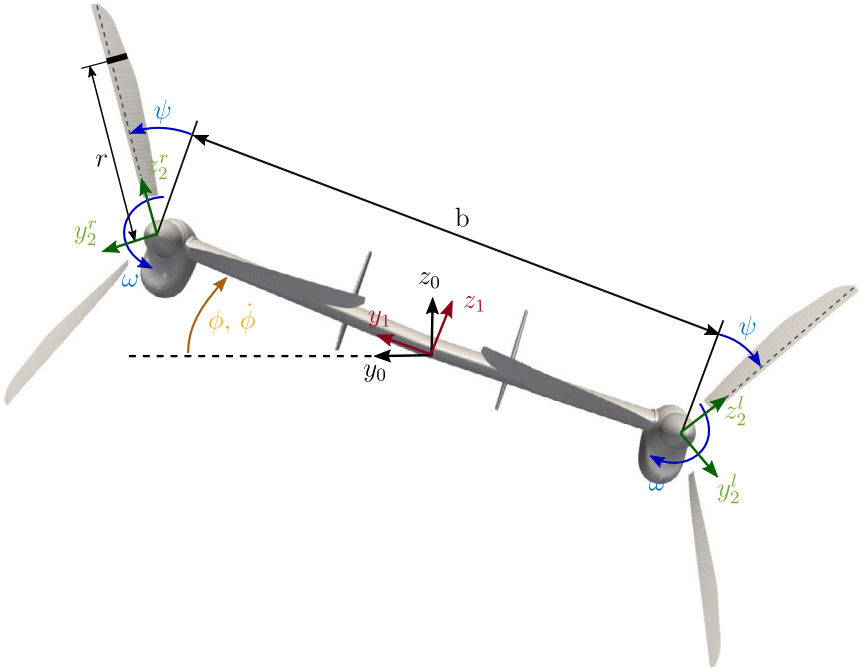

Fig. 22. Velocity components acting on rotors during roll maneuver; front view.

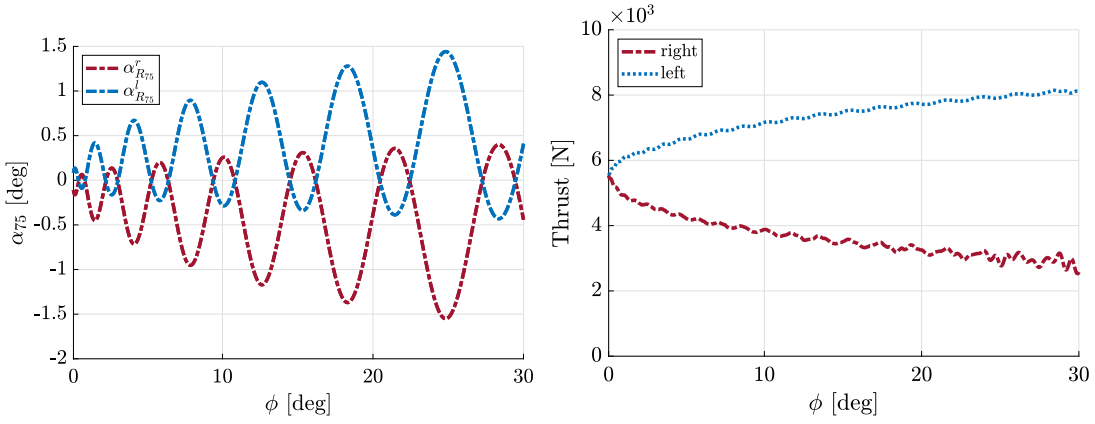

(a) α - Computed Angle of attack. (b) Thrust.

Fig. 23. Angle of attack (a) and thrust of the two rotors (b) for configuration II.

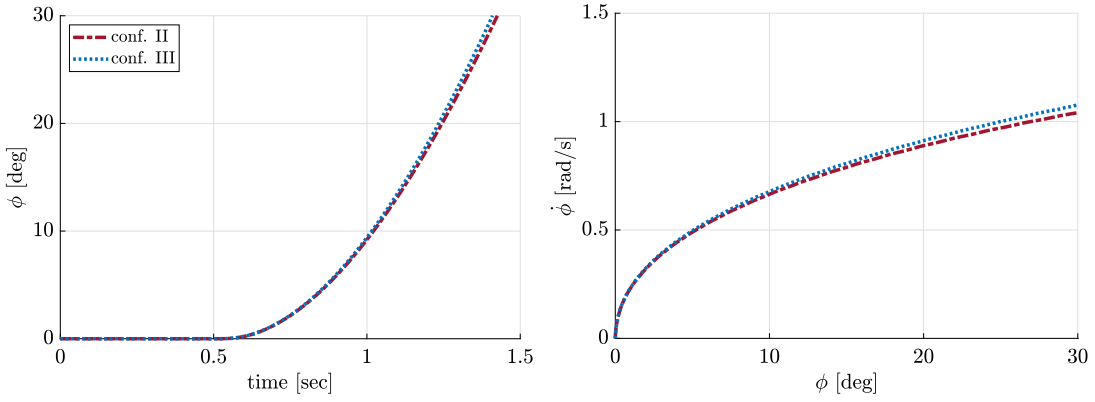

(a) Bank angle ϕ. (b) Roll rate p.

Fig. 24. Comparison of computed bank angle evolution (a), and roll rate evolution (b) for configurations II and III.

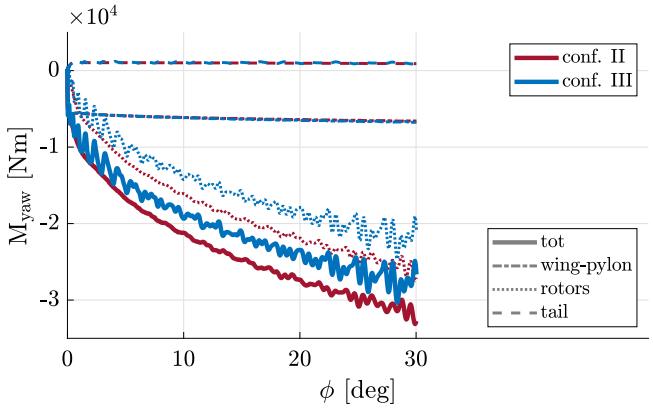

Fig. 25. Comparison of measured yaw moment for configurations II and III.

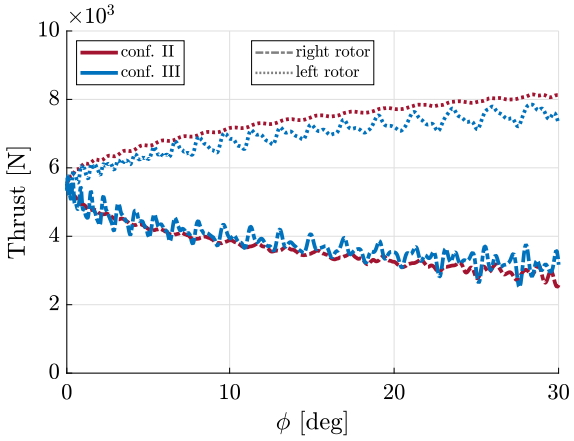

Fig. 26. Evolution during the maneuver of the measured thrust for the two proprotors, configuration III.

The tail is the only responsible for the generation of a proverse yaw. However, its contribution to the force breakdown is relatively small compared to other vehicle components.

5.2.2. Impact of rotor aerodynamic interaction

The next step considers Configuration III, which replaces the MBDyn rotor aerodynamics of Configuration II with the unsteady lifting lines of DUST, thus introducing the presence of the free wake of the two rotors in the model. The model coincides with *model B* used in Sec. 5.1.

When considering the roll performance, shown in Fig. 24, the aerodynamic interaction due to rotor wakes results in a reduction of the time to bank 30° of less than 2%. A significant impact is instead observed on the rotor loads and the resulting yaw moment (see Fig. 25). The rotors now generate a reduced adverse yaw moment compared to configuration II, although high-frequency oscillations due to the aerodynamic interactions between the wing and the rotors are observed. The time history of the thrust forces during the roll maneuver is shown in Fig. 26.

The blade pitch and flapping angles of the right rotor over an entire revolution are depicted in Fig. 27 during the initial maneuver phase and

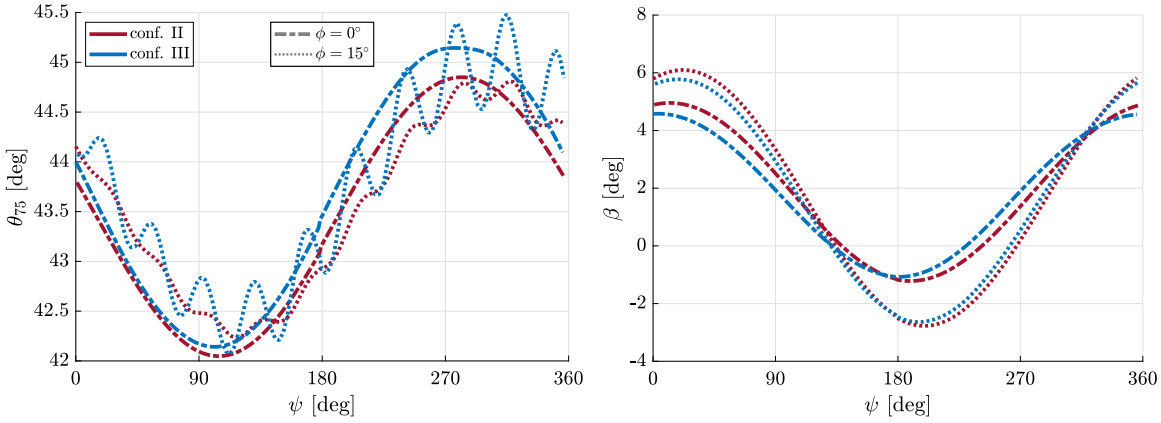

(a) Pitching angle. (b) Flapping angle.

Fig. 27. Comparison of right rotor pitch (θ_{75}) and flap (β) angles for configurations II and III, at different maneuver phases, $\phi = 0°$ and $\phi = 15°$.

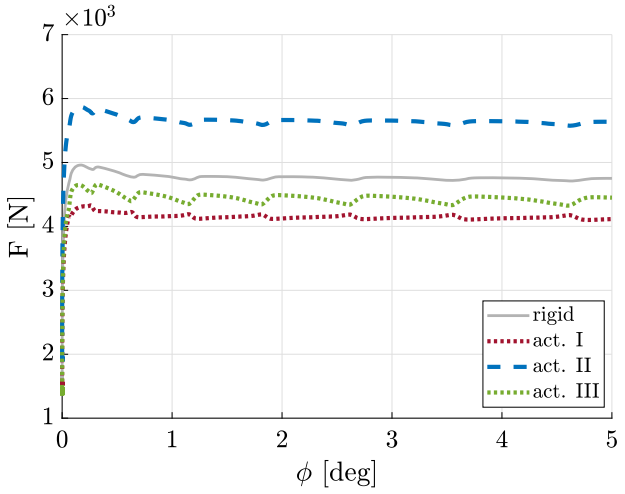

Fig. 28. Computed linear force on each actuator considering the flexible right flaperon during the first phase of the maneuver.

at a bank angle of $\phi = 15°$. As expected, the flapping angle increases its amplitude due to the lift asymmetry generated by the blades when increasing the roll rate. The evolution of the pitch angle, on the other hand, shows multiple harmonics that are more remarkable in Configuration III. In particular, the high-frequency harmonic activated during the maneuver corresponds to the second torsional mode of the blade at around $9/rev$. Hence, the aerodynamic forces in DUST provide less damping in the blade pitch motion when compared to BEMT aerodynamics, reducing rotor stability.

5.2.3. Impact of flaperon elasticity

Finally, the flexibility of the flaperon is taken into account. When considering a rigid control surface, the loads repartition on the 3 actuators remains the same. This is no longer valid when introducing the flexibility of the structure that modifies the hinge moment distribution and, consequently, the actuator forces.

The steady actuation force on the right flaperon during the roll maneuver is equal to 4900 N for configuration III. Indeed, all the 3 actuators provide the same force. The corresponding actuator forces when considering the elastic control surface are shown in Fig. 28. The maximum force ($\approx$ 5900 N) is generated by the centered actuator (act. II), leading to a 17% increment when compared to the rigid configuration. In contrast, the outer actuators show a force reduction of about 7% (act. II) and 13% (act. III).

Table 5
Computational time for the considered configurations to compute 1 sec of simulation.

	Conf. I	Conf. II	Conf. III	Conf. IV
Time	2 h 4 min	2 h 18 min	7 h 56 min	8 h 2 min

Although the mean force is similar to the value obtained with the rigid model, the analysis reveals that one actuator is more loaded than the others, and the corresponding force is higher than the one predicted by the rigid model. Consequently, the actuator design based on the rigid flaperon does not turn out to be conservative. From the perspective of the overall aircraft performance, i.e. bank angle, roll rate, and yaw moment, the results obtained with configuration IV are essentially identical to those of configuration III.

Finally, the computational time required to complete 1 sec of simulation for the different configurations analyzed is reported in Table 5, using a workstation with a Dual Intel® Xeon Gold 6230R @2.10 GHz processor with 52 physical cores and 2 threads for each core. As expected, the introduction of rotor aerodynamics in DUST leads to higher computational times, due to the presence of the free wake of the two rotors in the model.

6. Conclusions

This work proposes a new methodology for aeroelastic and aeromechanic analyses achievable with a comprehensive tool, that integrates the mid-fidelity aerodynamics of DUST and the multibody dynamics of MBDyn, for the evaluation of dynamic loads and performance indexes of new-generation VTOL aircraft.

By focusing on the analysis of a tiltrotor, a vehicle that encompasses the design challenges typical of both fixed- and rotary-wing aircraft, the flexibility of the numerical tool has been showcased.

To highlight the importance of including multiple details from the preliminary design phase, such as aerodynamic interactions, component flexibility, and system dynamics, different models with varying degrees of fidelity have been employed and compared. Preliminary results have been validated thanks to the extensive data available for the XV-15, demonstrating the capability of the tool to provide reliable outcomes when compared with high-fidelity tools and experimental tests.

Two analyses are then presented. Initially, the aircraft trim is obtained in steady-level flight. The approach allows us to determine both steady and periodic trim loads during forward flight conditions. Subsequently, starting from a specific trim condition, the roll maneuver of the aircraft is simulated, and transient loads on critical sections are evaluated and discussed.

Trim results demonstrate the critical role of modeling aerodynamic interactions in identifying periodic loads on different structural components. Indeed, vibratory loads play a pivotal role in optimizing aircraft design for safety and comfort. Roll maneuver simulations evidence how the inclusion of certain details in the preliminary numerical model such as rotor dynamics, interactional aerodynamics, actuation system dynamics, and component flexibility, allows for a more accurate estimation of the aircraft's performance indexes and transient loads. The information provided benefits the design of the aircraft control surfaces and the selection of the actuators. However, it must be stressed that mid-fidelity aerodynamic modeling, based on potential flow theory, has limitations in cases where the onset of separated regions associated with stall occurs. Therefore, the mid-fidelity approach can be used only in the regions of the aircraft flight envelope where the flow is attached.

Future developments of the mid-fidelity coupled tool will include the capability to generate reduced order models for control systems design and to perform fast aeroelastic stability analyses [57]. In addition, the first steps in using DUST for aeroacoustic analyses have been taken [58]. Indeed, aeroacoustic assessments are becoming a crucial aspect required for the design of the next-generation vertical take-off and landing vehicles in the upcoming contest of advanced air mobility.

CRediT authorship contribution statement

Alberto Savino: Conceptualization, Formal analysis, Investigation, Methodology, Software, Validation, Writing – original draft, Writing – review & editing, Visualization. **Alessandro Cocco:** Conceptualization, Formal analysis, Investigation, Methodology, Software, Validation, Writing – original draft, Writing – review & editing, Visualization. **Vincenzo Muscarello:** Conceptualization, Methodology, Validation, Writing – original draft, Writing – review & editing, Supervision.

Declaration of competing interest

The authors declare that they have no known competing financial interests or personal relationships that could have appeared to influence the work reported in this paper.

Data availability

Data will be made available on request.

References

[1] ACARE — Report of the Group of Personalities, European aeronautics: a vision for 2020, 2001.

[2] F.A. Administration, Noise Certification Standards for Tiltrotors, Technical Report, 2013, https://www.federalregister.gov/documents/2013/01/08/2013-00111/noise-certification-standards-for-tiltrotors.

[3] L. Pope, Propeller aircraft interior noise model utilization study and validation, Contractor Report 172428, NASA, 1984.

[4] Agenzia Nazionale per la Sicurezza del Volo, Accident occurred to the Agusta Westland AW609 aircraft registration marks N609AG, Technical Report, ANSV, 2015.

[5] S. Barkai, O. Rand, R. Peyran, R. Carlson, Modeling and analysis of tilt-rotor aeromechanical phenomena, Math. Comput. Model. 27 (1998) 17–43, https://doi.org/10.1016/S0895-7177(98)00071-5, https://www.sciencedirect.com/science/article/pii/S0895717798000715.

[6] W. Johnson, CAMRAD II, Comprehensive Analytical Model of Rotorcraft Aerodynamics and Dynamics, Volume I: Theory, Johnson Aeronautics, 1992.

[7] O.A. Bauchau, N.K. Kang, A multibody formulation for helicopter structural dynamic analysis, J. Am. Helicopter Soc. 38 (1993) 3–14, https://doi.org/10.4050/JAHS.38.2.3.

[8] H. Yeo, M. Potsdam, B. Ortun, K. Van Truong, High-fidelity structural loads analysis of the ONERA 7A rotor, J. Aircr. 54 (2017) 1825–1839, https://doi.org/10.2514/1.C034286.

[9] G.L. Ghiringhelli, P. Masarati, P. Mantegazza, M.W. Nixon, Multi-body analysis of a tiltrotor configuration, Nonlinear Dyn. 19 (1999) 333–357, https://doi.org/10.1023/A:1008386219934.

[10] G. Quaranta, P. Masarati, M. Lanz, G.L. Ghiringhelli, P. Mantegazza, M.W. Nixon, Dynamic stability of soft-in-plane tiltrotors by parallel multibody analysis, in: 26th European Rotorcraft Forum, The Hague, the Netherlands, 2000, 60.1–9.

[11] M. Mattaboni, P. Masarati, G. Quaranta, P. Mantegazza, Multibody simulation of integrated tiltrotor flight mechanics, aeroelasticity and control, J. Guid. Control Dyn. 35 (2012) 1391–1405, https://doi.org/10.2514/1.57309.

[12] A. Cocco, S. Mazzetti, P. Masarati, S. van 't Hoff, B. Timmerman, Numerical whirl-flutter analysis of a tiltrotor semi-span wind tunnel model, CEAS Aeronaut. J. 13 (2022) 923–938, https://doi.org/10.1007/s13272-022-00605-2.

[13] P. Masarati, M. Morandini, P. Mantegazza, An efficient formulation for general-purpose multibody/multiphysics analysis, J. Comput. Nonlinear Dyn. 9 (2014) 041001, https://doi.org/10.1115/1.4025628.

[14] H. Yeo, M. Potsdam, A. Ormiston Robert, Rotor aeroelastic stability analysis using coupled computational fluid dynamics/computational structural dynamics, J. Am. Helicopter Soc. 56 (2011) 1–16, https://doi.org/10.4050/JAHS.56.042003.

[15] M.J. Smith, J.W. Lim, B.G. van der Wall, J.D. Baeder, R. Biedron, D. Boyd, B. Jayaraman, S. Jung, B. Min, The HART II international workshop: an assessment of the state of the art in CFD/CSD prediction, CEAS Aeronaut. J. 4 (2013) 345–372, https://doi.org/10.1007/s13272-013-0078-8.

[16] A. Datta, J. Sitaraman, I. Chopra, J.D. Baeder, CFD/CSD prediction of rotor vibratory loads in high-speed flight, J. Aircr. 43 (2006) 1698–1709, https://doi.org/10.2514/1.18915.

[17] J. Sitaraman, B. Roget, Prediction of helicopter maneuver loads using a fluid-structure analysis, J. Aircr. 46 (2009) 1770–1784, https://doi.org/10.2514/1.43004.

[18] A. Altmikus, S. Wagner, P. Beaumier, G. Servera, A comparison - weak versus strong modular coupling for trimmed aeroelastic rotor simulations, in: AHS International, 58th Annual Forum Proceedings, vol. 1, 2002, pp. 697–710.

[19] W. Khier, M. Dietz, T. Schwarz, S. Wagner, Trimmed CFD simulation of a complete helicopter configuration, in: High Performance Computing in Science and Engineering, 2007, pp. 487–501.

[20] T. Guo, D. Lu, Z. Lu, D. Zhou, B. Lyu, J. Wu, CFD/CSD-based flutter prediction method for experimental models in a transonic wind tunnel with porous wall, Chin. J. Aeronaut. 33 (2020) 3100–3111, https://doi.org/10.1016/j.cja.2020.05.014, https://www.sciencedirect.com/science/article/pii/S1000936120302326.

[21] S. Massey, A. Kreshock, M. Sekula, Coupled CFD/CSD analysis of rotor blade structural loads with experimental validation, in: 31st AIAA Applied Aerodynamics Conference, San Diego, CA, USA, 2013.

[22] Y. Lu, T. Su, R. Chen, P. Li, Y. Wang, A method for optimizing the aerodynamic layout of a helicopter that reduces the effects of aerodynamic interaction, Aerosp. Sci. Technol. 88 (2019) 73–83, https://doi.org/10.1016/j.ast.2019.03.005.

[23] E. Alvarez, A. Ning, Development of a vortex particle code for the modeling of wake interaction in distributed propulsion, in: AIAA Applied Aerodynamics Conference, Atlanta, GA, 2018.

[24] J. Tan, T. Zhou, J. Sun, G. Barakos, Numerical investigation of the aerodynamic interaction between a tiltrotor and a tandem rotor during shipboard operations, Aerosp. Sci. Technol. 87 (2019) 62–72, https://doi.org/10.1016/j.ast.2019.02.005.

[25] M. Tugnoli, D. Montagnani, M. Syal, G. Droandi, A. Zanotti, Mid-fidelity approach to aerodynamic simulations of unconventional VTOL aircraft configurations, Aerosp. Sci. Technol. 115 (2021) 106804, https://doi.org/10.1016/j.ast.2021.106804, https://www.sciencedirect.com/science/article/pii/S127096382100314X.

[26] H.-J. Bungartz, F. Lindner, B. Gatzhammer, M. Mehl, K. Scheufele, A. Shukaev, B. Uekermann, preCICE – a fully parallel library for multi-physics surface coupling, Comput. Fluids 141 (2016) 250–258, https://doi.org/10.1016/j.compfluid.2016.04.003, http://www.sciencedirect.com/science/article/pii/S0045793016300974, advances in Fluid-Structure Interaction.

[27] A. Savino, A. Cocco, A. Zanotti, M. Tugnoli, P. Masarati, V. Muscarello, Coupling mid-fidelity aerodynamics and multibody dynamics for the aeroelastic analysis of rotary-wing vehicles, Energies 14 (2021) 6979, https://doi.org/10.3390/en14216979.

[28] C.W. Acree, An improved CAMRAD model for aeroelastic stability analysis of the XV-15 with advanced technology blades, TM 4448, NASA Ames Research Center, Mountain View, CA, 1993, https://ntrs.nasa.gov/search.jsp?R=19930013297.

[29] F.F. Felker, M.D. Betzina, D.B. Signor, Performance and Loads Data from a Hover Test of a Full-Scale XV-15 Rotor, Technical Report, NASA Ames Research Center, Moffett Field California, 1985.

[30] M.D. Betzina, Rotor performance of an isolated full-Scale XV-15 tiltrotor in helicopter mode, Technical Report, National Aeronautics and Space Administration Moffet Field CA Rotorcraft, 2002.

[31] S.W. Ferguson, W.F. Clement, W.B. Cleveland, D.L. Key, Assessment of simulation fidelity using measurements of piloting technique in flight, in: American Helicopter Society 40th Annual Forum, Arlington, VA, USA, 1984, pp. 67–92.

[32] G.H. Cottet, P.D. Koumoutsakos, Vortex Methods: Theory and Practice, Cambridge University Press, 2000.

[33] G.S. Winckelmans, Topics in vortex methods for the computation of three- and two-dimensional incompressible unsteady flows, Ph.D. dissertation, California Institute of Technology, 1989.

[34] K. Lindsay, R. Krasny, A particle method and adaptive treecode for vortex sheet motion in three-dimensional flow, J. Comput. Phys. 172 (2001) 879–907, https://doi.org/10.1006/jcph.2001.6862.

[35] R.E. Brown, A.J. Line, Efficient high-resolution wake modeling using the vorticity transport equation, AIAA J. 43 (2005) 1434–1443, https://doi.org/10.2514/1.13679.

[36] H. Zhang, R. Zhang, A. Zanoni, P. Masarati, Performance of implicit A-stable time integration methods for multibody system dynamics, Multibody Syst. Dyn. 54 (2022) 263–301, https://doi.org/10.1007/s11044-021-09806-9.
[37] P. Masarati, M. Morandini, Intrinsic deformable joints, Multibody Syst. Dyn. 23 (2010) 361–386, https://doi.org/10.1007/s11044-010-9194-y.
[38] G.L. Ghiringhelli, P. Masarati, P. Mantegazza, A multi-body implementation of finite volume C^0 beams, AIAA J. 38 (2000) 131–138, https://doi.org/10.2514/2.933.
[39] O.A. Bauchau, P. Betsch, A. Cardona, J. Gerstmayr, B. Jonker, P. Masarati, V. Sonneville, Validation of flexible multibody dynamics beam formulations using benchmark problems, Multibody Syst. Dyn. 37 (2016) 29–48, https://doi.org/10.1007/s11044-016-9514-y.
[40] M. Morandini, P. Masarati, Implementation and validation of a 4-node shell finite element, in: ASME IDETC/CIE 2014, Buffalo, NY, 2014, DETC2014-34473.
[41] R.R. Craig Jr., M.C.C. Bampton, Coupling of substructures for dynamic analysis, AIAA J. 6 (1968) 1313–1319, https://doi.org/10.2514/3.4741.
[42] M.D. Maisel, D.J. Giulianetti, D.C. Dugan, The History of the XV-15 Tilt Rotor Research Aircraft: From Concept to Flight, The NASA History Series, 2000, pp. 65–82, Washington, D.C.
[43] J.G. Leishman, Principles of Helicopter Aerodynamics, 2nd ed., Cambridge University Press, Cambridge, UK, 2006.
[44] P. Masarati, Direct eigenanalysis of constrained system dynamics, Proc. Inst. Mech. Eng., Part K, J. Multi-Body Dyn. 223 (2009) 335–342, https://doi.org/10.1243/14644193JMBD211.
[45] K. Bartie, H. Alexander, M. McVeigh, S. Lamon, H. Bishop, Hover performance tests of baseline metal and advanced technology blade (ATB) rotor systems for the XV-15 tilt rotor aircraft, Contractor Report 177436, NASA Ames Research Center, 1986.
[46] W. Johnson, Rotorcraft Aeromechanics, Cambridge University Press, New York, NY, USA, 2013, pp. 39–91.
[47] A. Cocco, A. Savino, P. Masarati, Flexible Multibody Model of a Complete Tiltrotor for Aeroservoelastic Analysis, International Design Engineering Technical Conferences and Computers and Information in Engineering Conference, vol. 86304, American Society of Mechanical Engineers, 2022, V009T09A026.
[48] S.W. Ferguson, A Mathematical Model for Real Time Flight Simulation of a Generic Tilt-Rotor Aircraft, CR 166536, NASA, 1988.
[49] C.W. Acree, R.J. Peyran, W. Johnson, Rotor design options for improving tiltrotor whirl-flutter stability margins, J. Am. Helicopter Soc. 46 (2001) 87–95, https://doi.org/10.4050/JAHS.46.87.
[50] A. Savino, A. Cocco, A. Zanoni, A. Zanotti, V. Muscarello, A coupled multibody-mid fidelity aerodynamic tool for the simulation of tiltrotor manoeuvres, in: 47th European Rotorcraft Forum, Virtual Event, 2021.
[51] H.E. Merritt, Hydraulic Control Systems, John Wiley & Sons, New York, 1967.
[52] T.H.G. Megson, Aircraft Structures for Engineering Students, Butterworth-Heinemann, 2016.
[53] A. Savino, A Mid-Fidelity Aeroelastic Environment for Tiltrotor Analysis and Design, Phd thesis, Politecnico di Milano, Milan, via La Masa 34, 2023, https://hdl.handle.net/10589/207272.
[54] T.D. Economon, F. Palacios, S.R. Copeland, T.W. Lukaczyk, J.J. Alonso, Su2: an open-source suite for multiphysics simulation and design, AIAA J. 54 (2016) 828–846, https://doi.org/10.2514/1.J053813.
[55] V. Muscarello, G. Quaranta, Structural coupling and whirl-flutter stability with pilot-in-the-loop, J. Am. Helicopter Soc. 66 (2021) 1–16, https://doi.org/10.4050/JAHS.66.032003.
[56] S.W. Ferguson, A Mathematical Model for Real Time Flight Simulation of a Generic Tilt-Rotor Aircraft, CR 166536, NASA, 1988.
[57] N. Böhnisch, C. Braun, V. Muscarello, P. Marzocca, About the wing and whirl flutter of a slender wing-propeller system, J. Aircr. (2024) 1–14, https://doi.org/10.2514/1.C037542.
[58] F. Caccia, L. Abergo, A. Savino, M. Morelli, B.Y. Zhou, G. Gori, A. Zanotti, G. Gibertini, L. Vigevano, A. Guardone, Multi-fidelity numerical approach to aeroacoustics of tandem propellers in eVTOL airplane mode, in: AIAA AVIATION 2023 Forum, 2023, p. 3221.